Received: 18 November 2022 | Revised: 08 January 2023 | Accepted: 14 January 2023
DOI: 10.22034/ecc.2023.370745.1556
Journal of Medicinal and Pharmaceutical Chemistry Research
SAMI

FULL PAPER

Iron (II), cobalt (II), and nickel (II) complexes of bis- (3-chloroacetylacetonate) ethylenediimine and bis-(acetylacetonate) ethylenediimine and their viologen molecular switches

Akram Muhamed Musaa[a,b,*] | Wathiq Star Abdul-Hassan[a]

[a]*Department of Chemistry, College of Science, University of Thi-Qar, 64001 Nassiria, Iraq*

[b]*Thi-Qar General Directorate of Education, 64001 Nassiria, Iraq*

Corresponding Author:
Akram Muhamed Musaa
Email: akrammuhamed@yahoo.com
Tel.: +96416104164

Preparation of AAN and ACl is performed by reaction 1 equivalent of en and 2 equivalents of acetyl acetone and 3-chloro acetyl acetone, respectively. Fe^{2+}, Co^{2+}, and Ni^{2+}complexes with both bis(acetylacetone) ethylenediimine AAN and bis(3-chloroacetylacetone) ethylenediimine ACl ware synthesized. The adduct complex $[Fe(AAN)(bpy)_2]$ was also synthesized from reaction of $[Fe(AAN)(H_2O)_2]$ with 4,4′-bipyridine. These N_2O_2 metal complexes have been characterized by FT-IR, UV-Vis, and TG analysis as well as XRD spectrometries. Interaction of 4,4′-bipyridine (bpy) with metal (II) complexes in solution affords adduct complexes, i.e. through coordination of bpy with metal ion (II). Interaction of $V_2^{2+}.2PF_6^-$ with metal (II) complexes in solution affords adduct complexes, i.e. through coordination of $V_2^{2+}.2PF_6^-$ with metal ion (II). The solutions of adduct complexes happened among bis-viologen $V_2^{2+}.2PF_6^-$ and metal complexes have been reduced by activated zinc powder to afford viologen-based molecular switches.

KEYWORDS

Bis(acetylacetone) ethylenediimine; bis(3-chloroacetylacetone) ethylenediimine; adduct; 4,4′– bipyridine; viologen switches; metal (II) complexes.

Introduction

A Schiff base, named after Hugo Schiff, is a molecule containing a functional group with a carbon-nitrogen double bond, but with the nitrogen atom connected to an aryl or alkyl group instead of hydrogen [1]. After combining two moles of acetylacetone and one mole of ethylenediamine, the resulting Schiff base bis(acetylacetonyl)ethylenediimine [4,4-(1,2 ethanediyldinitrilo)-bis(2-pentanone)] was found to have an enaminoketone structure with intramolecular hydrogen bonding in both solid state and solution [2]. The large work on investigation of transition elements complexes made from Schiff bases has been developed in recent years due to the selectivity and high sensitivity of Schiff bases towards a range oftransition metal ions. Schiff bases metal complexes have been known for more than a century [3-6]. Ligands complexes can act as bidentate or tridentate depending on the presence of azomethine, an active donor group that can share the electron pair of a nitrogen atom in the formation of coordination bond, or other donating groups in compounds of transparent bases like oxygen or sulfur [7]. Tridentate, tetradentate, and polydentate homogeneous

or heterogeneous bases, as well as their metal complexes, have a wide range of potential uses [2]. As Schiff bases can coordinate to divalent metal ions, research into these compounds is of great significance. When thinking about these Schiff bases, it is important to take into account the positions of the keto-enol or amine-imine equilibrium and the nature of hydrogen bond in the six-membered chelate ring [8]. In the case of bis-(acetylacetone)-ethylenediimine, the I–III forms could exist in tautomeric equilibrium, as shown by the Scheme 1.

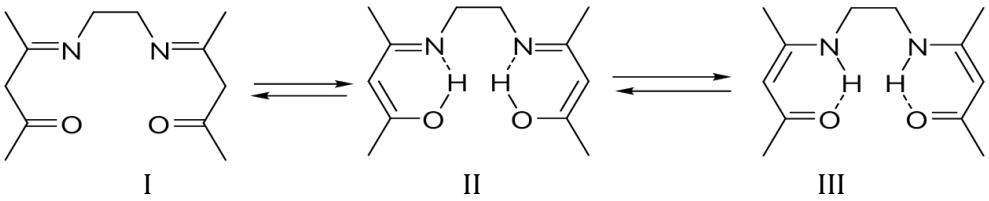

I II III

SCHEME 1 Tautomeric equilibrium of bis (acetylacetonyl) ethylenediimine

The purpose of this work was to examine the formation of adduct complexes between bis (acetylacetonato) ethylenediimine Co(II), Fe(II), Ni(II), bis (3-chloro acetylacetonato) ethylenediimine Fe(II) with 4,4'-bipyridine (solids and solutions), and dicationic propylene-spacered bis-viologen $V_2^{2+}.2PF_6^-$. Then, promoting the formation of molecular switches based on the adduct complexes with $V_2^{2+}.2PF_6^-$ was performed.

Experimental

Solvents and reagents

All solvents and chemical reagents are commercially sourced and used without further purification.

Instrumentation

FT-IR spectra ware recorded using BRUKER /FT-IR Affinity-1 spectrophotometer and KBr disks. UV-Visible absorption spectra ware recorded on a T90+ UV-visible spectrometer (PG Instruments Ltd) using conventional quartz cell having an optical path length of 1 cm. Melting points of the prepared compound were measured using melting points/SMP3 apparatus Department of Chemistry, College of Science, University of Thi-Qar, Iraq. Thermal analysis was recorded on TGA-50 in Department of Chemistry, College of Education for pure Science University of Basra. The XRD measurements were carried out using Panalytical diffractometer with Cu Ka radiation, in Department of Chemistry, College of Education for pure Science, University of Basra. ^{1}H-NMR spectra ware recorded by BRUKER spectrophotometer (500 MHz) in Department of Chemistry, Tehran University, Iran, using DMSO-d_6 and D_2O as solvents. Mass spectra ware recorded using 5973 Network Mass Selective Detector manufactured by Agilent Technology (HP) with ion source of Electron Impact (EI) 70 ev in Department of Chemistry, Tehran University, Iran.

Syntheses of bis (acetylacetone) ethylenediimine (AAN) and bis (3-chloroacetylacetone) ethylenediimine (ACl)[9,10]

Ethylenediamine (1.75 mL, 1.575 g, 26.25 mmol) or (0.59 mL, 0.531 g, 8.85 mmol) in 1 mL ethanol was added with stirring in a dropwise manner into solution of acetylacetone (5.38 mL, 5.25 g, 52.5 mmol) or 3-chloroacetylacetone (2 mL, 2.38 g, 17.7 mmol), respectively, in ethanol (1 mL) placed in ice bath. The resulting mixtures ware stirred in the ice bath for 1 hour, and then at lab temperature for 24 hours. The reaction mixture of AAN was left to dry under air atmosphere. The produced precipitate of

crude ACl was collected by filtration. The crude AAN precipitate was recrystallized from water and washed with diethylether. The crude ACl precipitate was washed with diethylether and then with water. Both precipitates ware dried under vacuum to afford AAN as light yellow-white solid and ACl as light yellow solid in yields of 4.6 g, 69 %, (M.P = 117 °C) and 1.11 g, 43% (M.P = 130 °C), respectively. FT-IR, cm^{-1} (AAN): 3163 υO-H, 3088 υC-H of C=C-H, 2988, 2957, 2915 υC-H, 1616 υC=N, 1567 υC=C, 1326 aliphatic C-H bending, 1184 υC-O, and 768 υC-H bending of C=C-H. FT-IR, cm^{-1} (ACl): 3133 υO-H, 3059 υC-H of C=C-H, 2991, 2958, 2920 υC-H, 1596 υC=N, 1562 υC=C, 1361 aliphatic C-H bending, 1218 υC-O, 787 υC-Cl, and 667 υC-H bending of C=C-H. ^{1}H-NMR (500 MHz, DMSO-d6), δ (ppm): 11.19 (d, 2H, H_a), 3.50 (d, 4H, H_b), 2.15 (d, 12H, H_c). EI-MS (m/z) = 292$[M]^{+}$, 257 $[M-Cl]^{+}$, 192 $[M-2Cl]^{+}$, 146 $[M/2]^{+}$(Scheme 2).

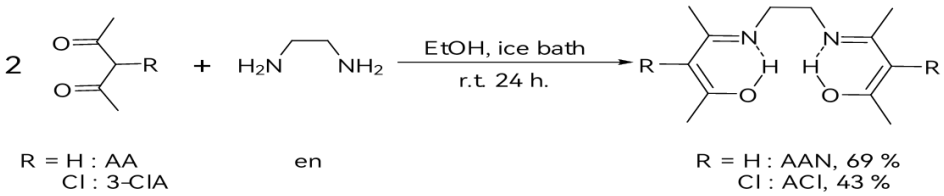

SCHEME 2 Syntheses of AAN and ACl

Syntheses of complexes

Synthesis of [Ni(AAN)]

3.265 g, 8.9 mmol of nickel (II) perchlorate hexahydrate dissolved in 1 mL of methanol was added gradually to 2 g, 8.9 mmol of AAN dissolved in 4 mL of methanol. The reaction mixture was heated at 80 °C for 1 hour. The produced precipitate was collected by hot filtration, washed with distilled water and methanol, respectively, and dried under vacuum to afford the complex as red in yield of 1.3 g, 52%. M.P =233 °C. FT-IR: 2984, 2951, 2915, 2851 υC-H, 2063 υC-H of C=C-H, 1584 υC=C, 1518 υC=N, 1364 aliphatic C-H bending, 1109 υC-O, 778 υC-H bending of C=C-H and 428 υNi-N (Scheme 3).

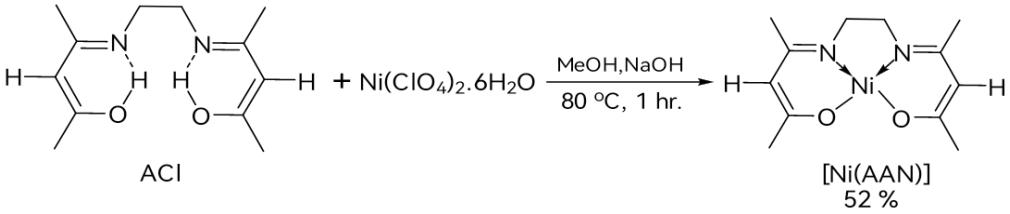

SCHEME 3 Synthesis of [Ni(AAN)]

Syntheses of $[Co(AAN)(H_2O)_2]$, $[Fe(AAN)(H_2O)_2]$, and $[Fe(ACl)(H_2O)_2]$

AAN (2 g, 8.9 mmol) dissolved in 50 mL or 28 mL distilled water or ACl (2 g, 6.8 mmol) dissolved in 28 mL methanol was added separately to a solution 0.32 g, 8 mmol of NaOH in 5 mL of distilled water. The last solutions ware added respectively to 2.1 g, 8.9 mmol of $CoCl_2.6H_2O$ in 9 mL of distilled water, 1.9 g, 8.6 mmol of $FeCl_2.6H_2O$ in 34 mL of distilled water and 1.6 g, 6.8 mmol of $FeCl_2.6H_2O$ in 32 mL of distilled water. The reaction mixture ware heated at 80 °C with stirring for 1 hour. The resulted precipitates were collected by filtration, washed with distilled water and then with methanol, and dried under vacuum. The obtained complexes: $[Co(AAN)(H_2O)_2]$ as green solid, $[Fe(AAN)(H_2O)_2]$ and $[Fe(ACl)(H_2O)_2]$ as red solid ware in yields of 1.5 g, 56%. (M.P =222 °C), 1.1 g, 41% (M.P =217 °C), and 1 g, 39% (M.P =235 °C), respectively. FT-IR, cm^{-1}

[Co(AAN)(H2O)2]: 3500 H2O stretching, 2968, 2925 υC-H, 1645 υC=N, 1564 υC=C, 1408 aliphatic C-H bending, 1117 υC-O, 828 υC-H bending of C=C-H and 425 υCo-N. FT-IR, cm-1 [Fe(AAN)(H2O)2]: 3391 H2O stretching, 3011 υC-H of C=C-H, 2989, 2947 υC-H, 1609 υC=N, 1571 υC=C, 1373 aliphatic C-H bending, 1136 υC-O, 845 υC-H bending of C=C-H and 424 υFe-N. FT-IR, cm-1 [Fe(ACl)(H2O)2]: 3363 H2O stretching, 3006 υC-H of C=C-H, 2967, 2927 υC-H, 1645 υC=N, 1561 υC=C, 1334 aliphatic C-H bending, 1041 υC-O, 915 υC-H bending of C=C-H, 688 υC-Cl, and 437 υFe-N (Scheme 4).

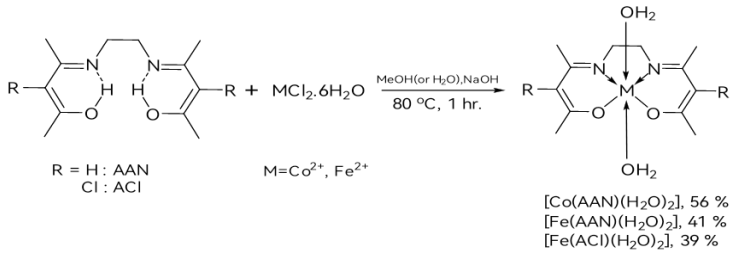

SCHEME 4 Synthesis of [M(AAN)(H2O)2], M= Co2+, Fe2+, and [Fe(ACl)(H2O)2]

[Fe(AAN)(bpy)2]

4,4′- Bipyridine (0.59 g, 3.83 mmol, 5 equivalents) was added to 0.2 g, 0.77 mmol, 1 equivalent of [Fe(ACl)(H2O)2] dissolved in the minimum amount of acetonitrile. The mixture solution was stirred at lab temperature for 24 hours. The resulted precipitate was collected by filtration and washed with acetonitrile to afford [Fe(AAN)(bpy)2] as red solid in yield of 0.09 g, 21% (M.P=203 °C).

Results and discussion

1H-NMR spectrometry of ACl

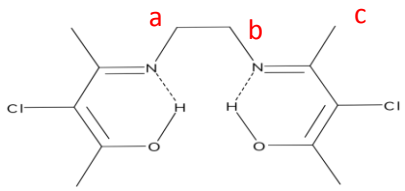

The compound ACl is characterized by 1H-NMR spectroscopy (500 MHz, DMSO- d6). The 1H-NMR signals of ACl as strong hydrogen bonded enol imino form $(-O-H\ldots\ldots N=C-)$ can be divided into three main regions which are: the signal of OH group (H_a), the signal of CH_2 groups (H_b), and the signal of CH_3 groups (H_c). The HOD signal should be noted at 3.33 ppm, but here it was noted at 3.53 ppm because H atom of HOD is hydrogen bonded to the ACl ligand. The 1H-NMR spectrum is depicted in Figure 1. The 1H-NMR assignments are shown in experimental.

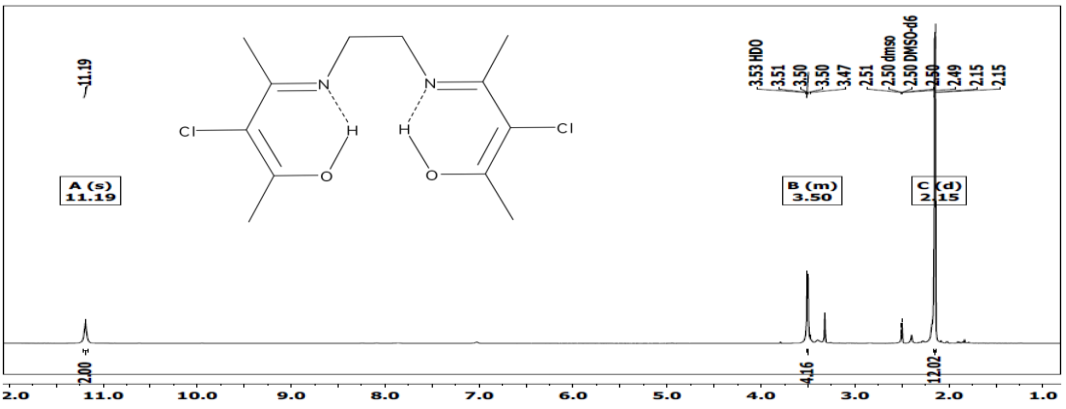

FIGURE 1 1H-NMR spectrum (500 MHz, DMSO- d6, 298K) of ACl

Mass spectrometry of ACl

The electron impact mass spectrum (EI-MS) of ACl showed a peak at m/z = 292 due to the molecular ion. The appearance of a peak at m/z = 257 indicates the loss of $Cl^{\cdot}$ radical. The spectrum showed an intensive peak at m/z = 146 due to loss half of compound. The peak at m/z = 192 is attributed to loss of two $Cl^{\cdot}$ radicals and two methyl groups. Other important peaks occurred at m/z =214, 192, 163, 127, 113, 104, 99, 57, and 43, as depicted in Figure 2.

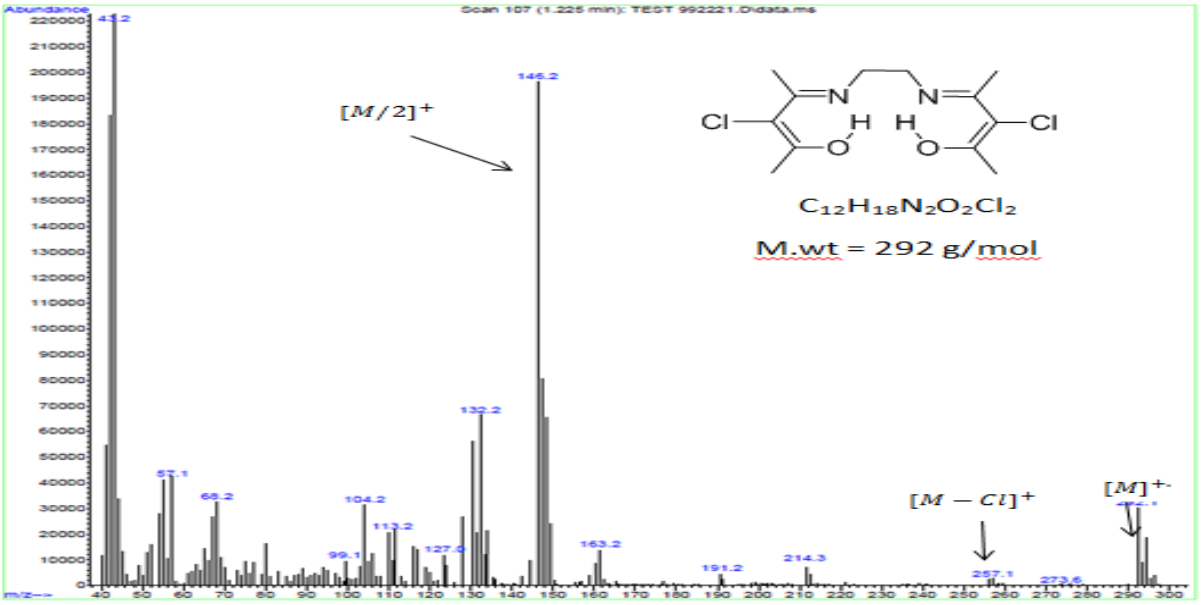

FIGURE 2 Electron impact mass spectrum (EI-MS) of ACl

FT-IR spectrometry

The FT-IR spectra of AAN and ACl and the complexes are shown in Figures 3-8. Their assignments are illustrated in experimental. The ligands AAN and ACl spectra showed hydrogen bonded O-H stretching vibrations and O-H bending disappeared in the complexes spectra. This refers to the complex deprotonation upon the complexation with metal (II) ions. Except the complex [Ni(AAN)], the Co (II) and Fe(II) complexes showed the broad coordinated H_2O stretching vibrations. Both ligands and complexes showed aromatic and aliphatic C-H stretching vibrations with their bending vibrations. The stretching vibrations of C=N, C=C, and C-O groups noted in FT-IR spectra are shifted compared with those in their ligands [11-14].

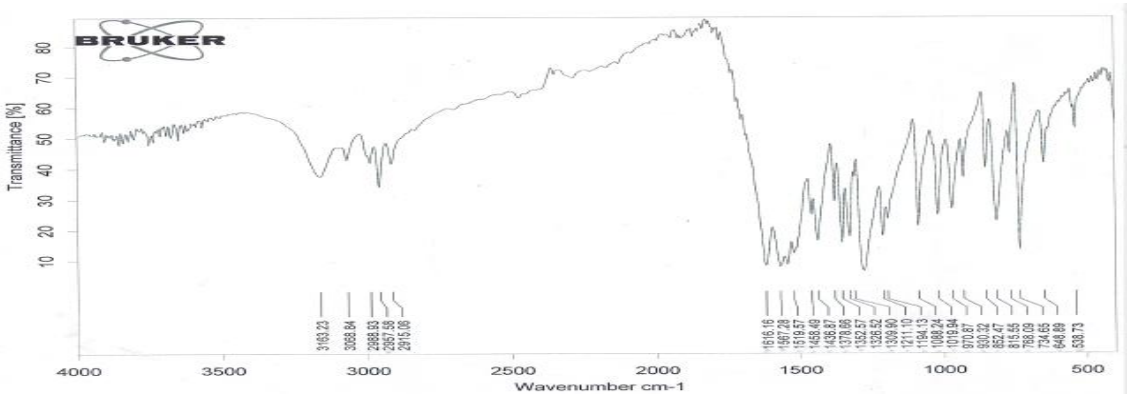

FIGURE 3 FT-IR spectrum of AAN

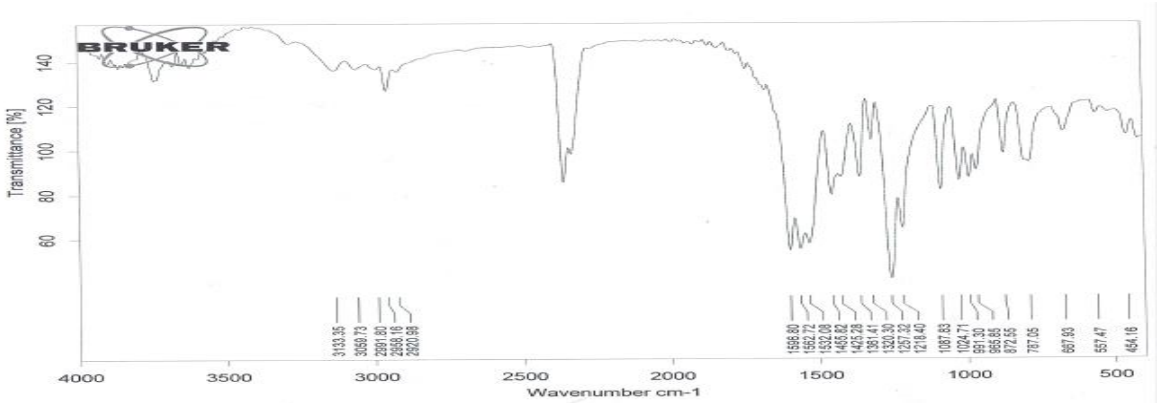

FIGURE 4 FT-IR spectrum of ACl

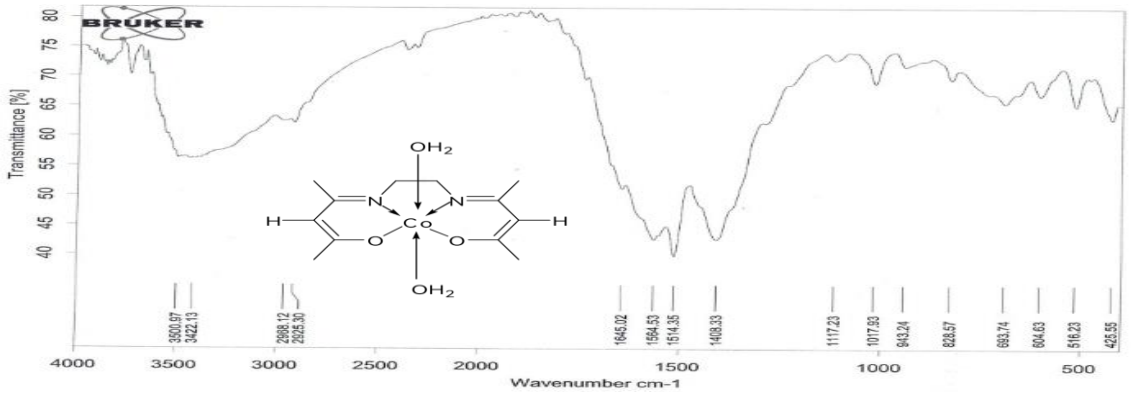

FIGURE 5 FT-IR spectrum of $[Co(AAN)(H_2O)_2]$

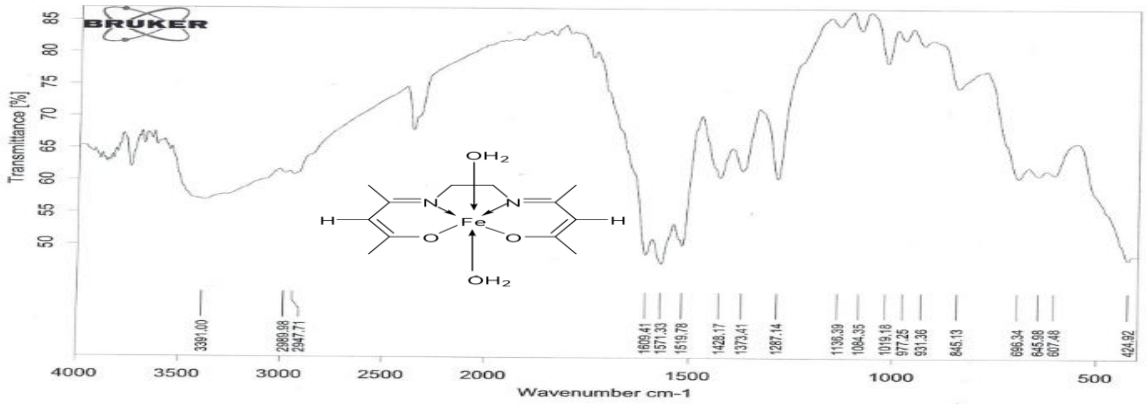

FIGURE 6 FT-IR spectrum of $[Fe(AAN)(H_2O)_2]$

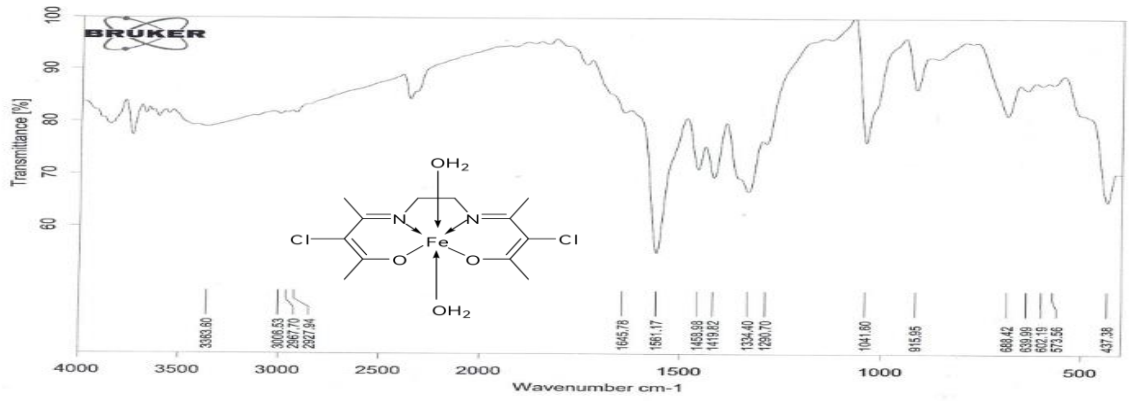

FIGURE 7 FT-IR spectrum of $[Fe(AN\text{-}Cl)(H_2O)_2]$

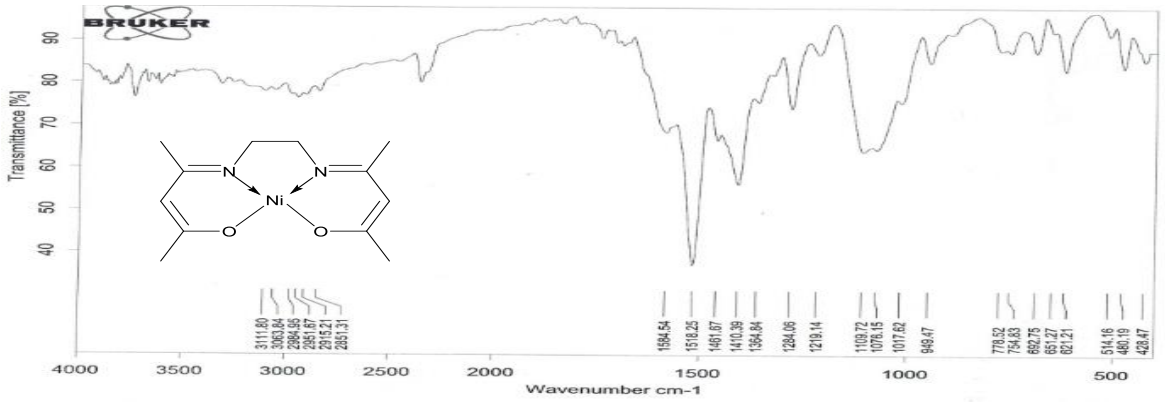

FIGURE 8 FT-IR spectrum of [Ni(AAN)]

Thermal analyses [7,16]

The thermal behavior of the complexes was studied using thermogravimetric analysis (TGA) that was recorded in nitrogen gas at heating rate of 20 °C/min. These TG curves are shown in Figures 9-12. The TG data and their assignments are listed in Table 8. The thermal decompositions started at 139.95 °C, 154.4 °C, 160.22 °C, and 173.62 °C for the complexes $[Co(AAN)(H_2O)_2]$, $[Fe(AAN)(H_2O)_2]$, [Ni(AAN)], and $[Fe(ACl)(H_2O)_2]$, respectively. The complex $[Co(AAN)(H_2O)_2]$ losses only two water molecules within temperature range 139.95-208.61 °C and starts decomposition at 251.43 °C. Then, the complex $[Co(AAN)(H_2O)_2]$ has the highest thermal stability within the other complexes. Therefore, the thermal stability increases in the sequence: $[Fe(AAN)(H_2O)_2]$ < [Ni(AAN)] < $[Fe(ACl)(H_2O)_2]$ < $[Co(AAN)(H_2O)_2]$.

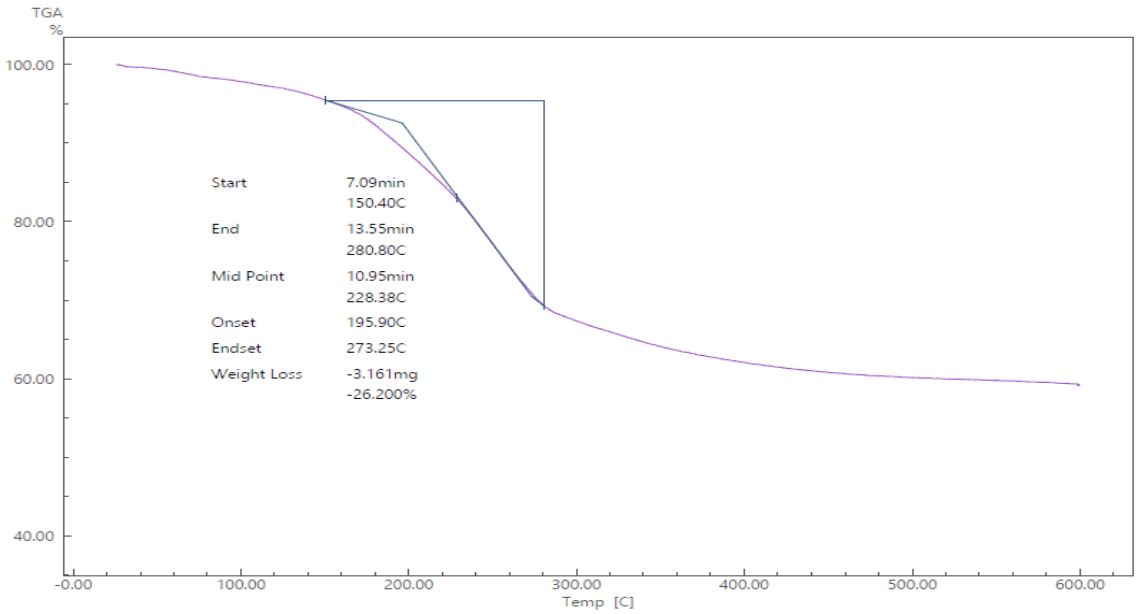

FIGURE 9 TGA of $[Fe(AAN)(H_2O)_2]$

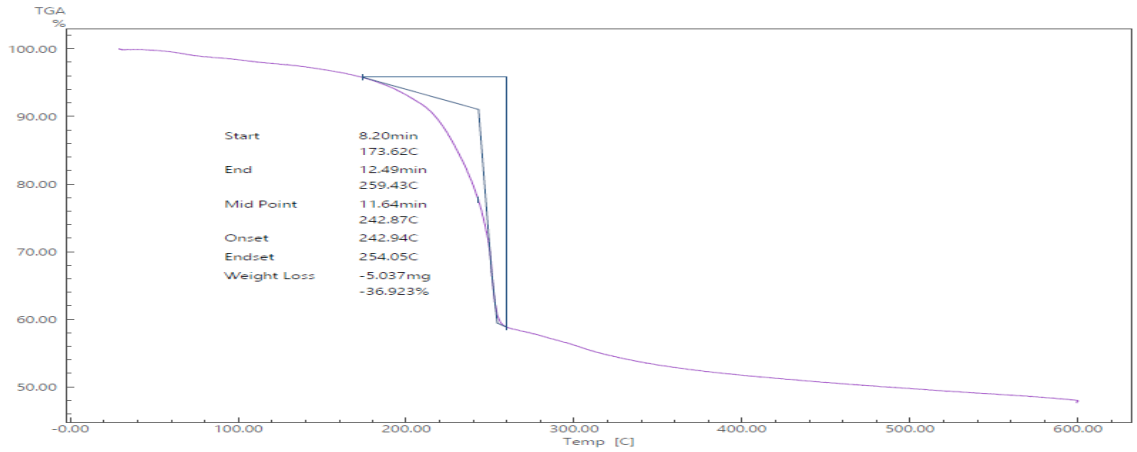

FIGURE 10 TGA of $[Fe(ACl)(H_2O)_2]$

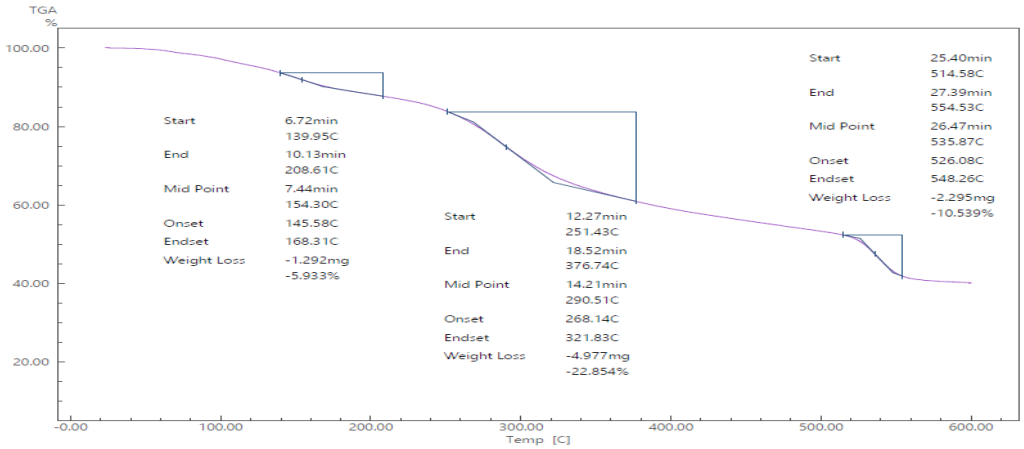

FIGURE 11 TGA of $[Co(AAN)(H_2O)_2]$

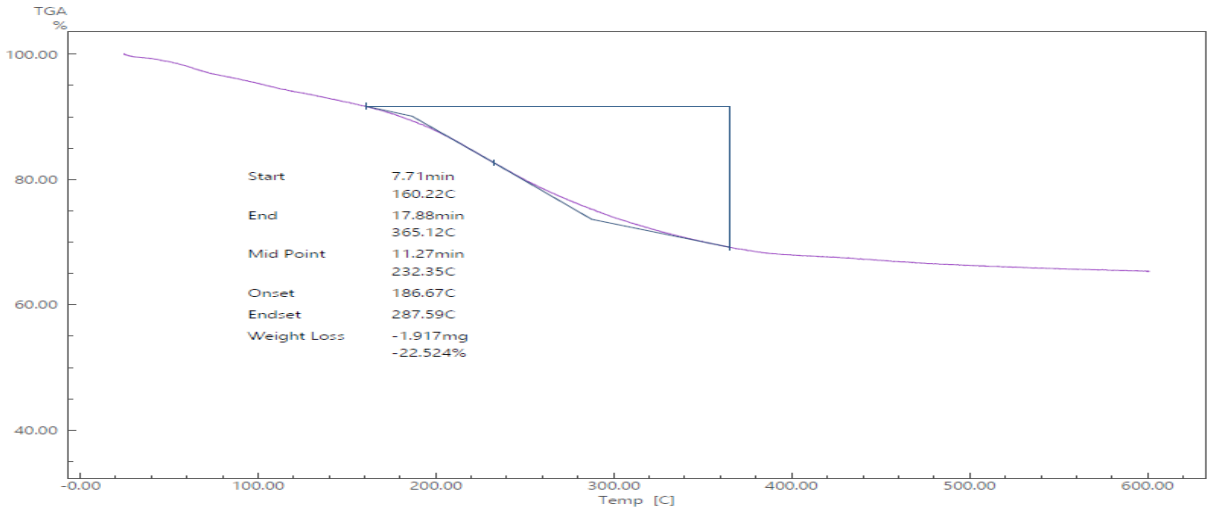

FIGURE 12 TGA of [Ni(AAN)]

TABLE 1 Thermogravimetric analysis data and their assignments of the complexes

Complex	Temperature range, °C	Molecular weight loss %		Missing part	Residual part
		Found	Calculated		
[Fe(AAN)(H₂O)₂]	150.4-280.8	26.2	25.16	$2H_2O+CH_3CO$	$FeC_{10}H_{15}N_2O$
[Fe(ACl)(H₂O)₂]	173.62-259.43	36.923	35.16	$2H_2O+2Cl+C_2H_4$	$FeC_{10}H_{12}N_2O_2$
	139.95-208.61	5.933	5.68	H_2O	$CoC_{12}H_{20}N_2O_3$
[Co(AAN)(H₂O)₂]	251.43-376.74	22.854	24.7	$H_2O+2\ C_2H_4$	$CoC_8H_{10}N_2O_2$
	514.58-554.53	10.539	12.4	C_2H_4	$CoC_6H_6N_2O_2$
[Ni(AAN)]	160.22-365.12	22.524	20	$2C_2H_4$	$NiC_8H_{10}N_2O_2$

Calculation of rate constant, half –time and thermodynamic parameters from TGA analysis

Considering all phase transformations as the 1st order reactions, activation energy and other thermodynamic parameters are determined using the 1st order reaction rate equation, as given in Equation (1).

$$\frac{dx}{dt} = k(1-x) \quad (1)$$

$$x = \frac{w_i - w_t}{w_i - w_f} \quad (2)$$

Where, w_i is the initial weight, w_t is weight of sample at particular time t, and w_f is final weight. Equation (1) can be rewritten as:

$$ln\ ln\ (1-x) = -kt \quad (3)$$

By plotting Equation 3, straight line is obtained for each individual phase, which confirmed that transformations are the first order reactions. Slope of each line give the value of rate constant (k) for particular phase (Figure 13). Half-life ($t_{\frac{1}{2}}$) was determined using Equation 4.

$$t_{\frac{1}{2}} = \frac{0.693}{k} \quad (4)$$

Values of k, $t_{\frac{1}{2}}$, activation energy, ΔH, ΔS, and ΔG are given in Table 2. Values obtained for each phase proved that all phases are non-spontaneous endothermic reactions.

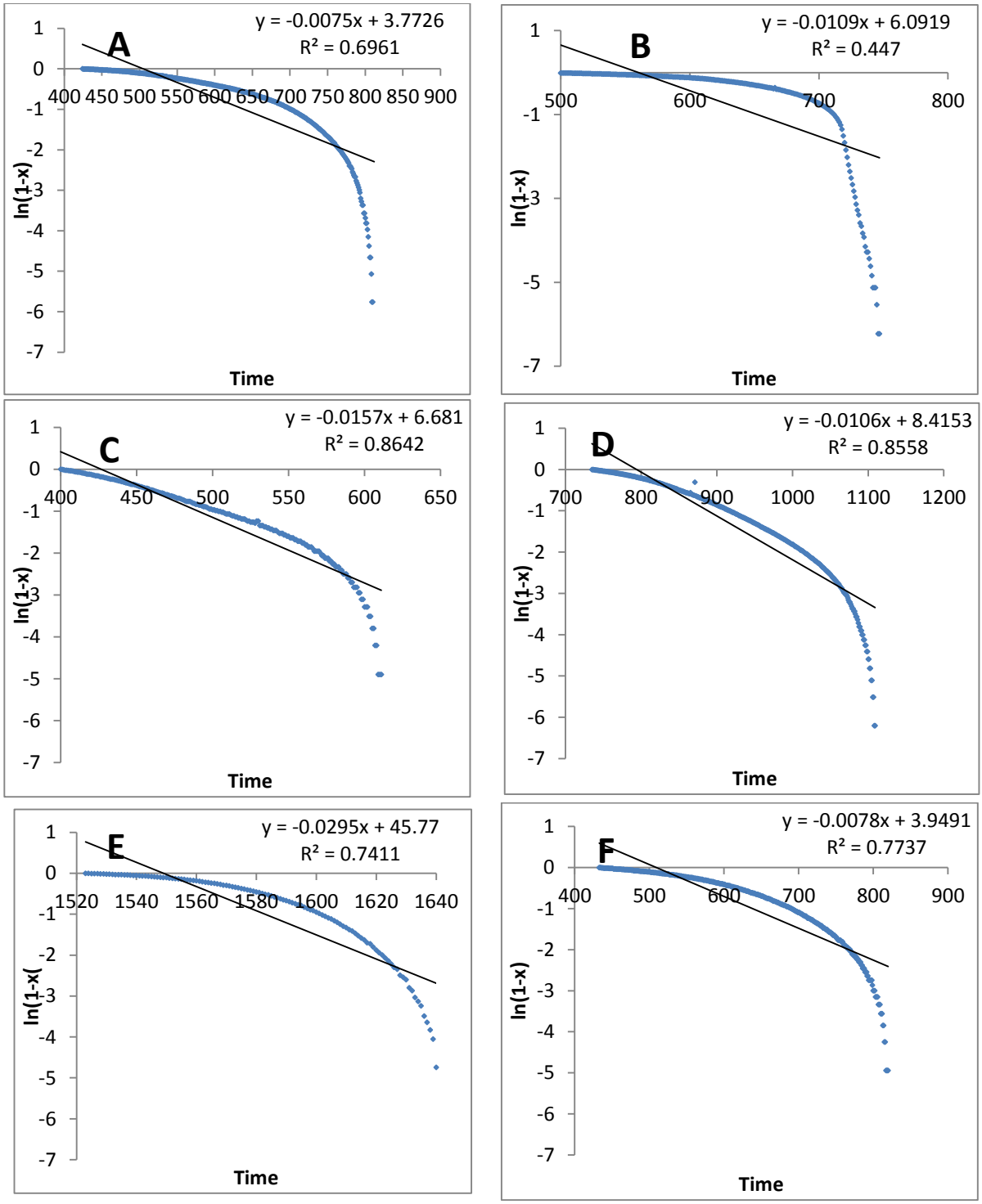

FIGURE 13 Plot of ln(1-x) vs. Time (sec) for loss weight of (A) [Fe(AAN)$(H_2O)_2$], (B) [Fe(ACl)$(H_2O)_2$], (C) the first phase of [Co(AAN)$(H_2O)_2$], (D) the 2nd phase and of [Co(AAN)$(H_2O)_2$], (E) the 3rd phase of [Co(AAN)$(H_2O)_2$], and (F) [Ni(AAN)]

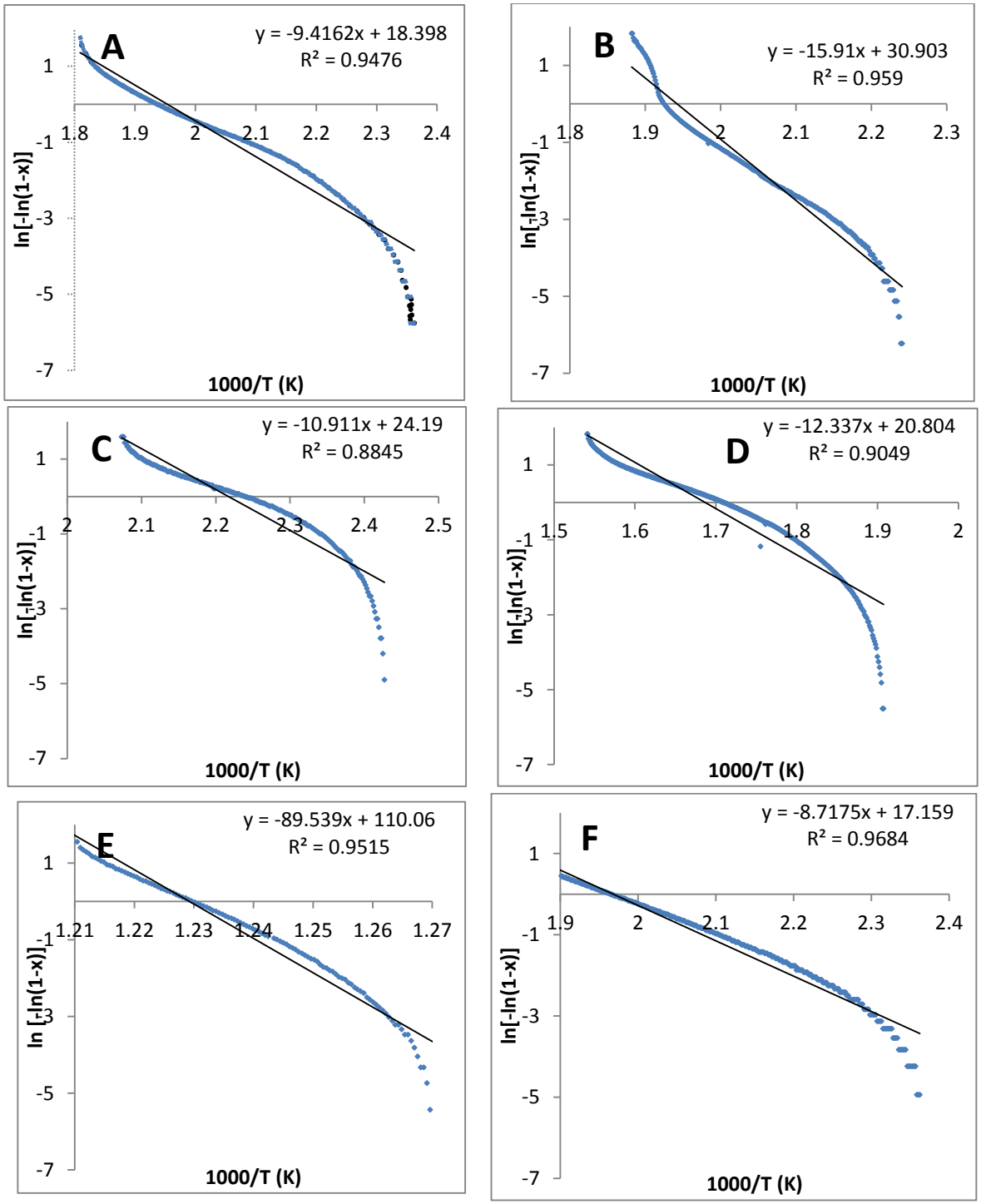

FIGURE 14 Plot of ln[-ln(1-x)] vs. 1000/T(K) for loss weight of (A) $[Fe(AAN)(H_2O)_2]$, (B) $[Fe(ACl)(H_2O)_2]$,(C) the first phase of $[Co(AAN)(H_2O)_2]$, (D) the 2nd phase of $[Co(AAN)(H_2O)_2]$, (E) the 3rd phase of $[Co(AAN)(H_2O)_2]$, and (F) [Ni(AAN)]

TABLE 2 Kinetic and thermodynamic parameters of each phase during thermogravimetric analysis of $[Fe(AAN)(H_2O)_2]$, $[Fe(ACl)(H_2O)_2]$, $[Co(AAN)(H_2O)_2]$, and [Ni(AAN)]

Complex	Phase	Temp (K)	K (min^{-1})	$t_{1/2}$ (sec)	E_a ($J\ mol^{-1}$) ($*10^3$)	ΔH ($J\ mol^{-1}$) ($*10^3$)	ΔS ($J\ mol^{-1}\ K^{-1}$)	ΔG ($J\ mol^{-1}$) ($*10^3$)
$[Fe(AAN)(H_2O)_2]$	first phase	554	0.0075	92.4	78.2563	736.504	-135.196	148.548
$[Fe(ACl)(H_2O)_2]$	first phase	533	0.0109	63.6	132.275	127.844	-25.9013	141.649
$[Co(AAN)(H_2O)_2]$	first phase	482	0.0157	44.1	90.7140	86.7067	-82.3405	126.394
	2nd phase	650	0.0106	65.4	102.569	97.1657	-116.929	173.169
	3ed phase	828	0.0295	23.5	744.427	737.543	635.5875	211.276
[Ni(AAN)]	first phase	628	0.0078	88.8	72.477	67.2561	-149.262	160.992

Kinetics parameters are determined using modified form of Coats and Redfern model, as described in Equation (5).

$$ln\ ln\ [-\ ln\ ln\ (1-x)\ ]\ = ln\frac{ART^2}{\beta E_a} - \frac{E_a}{RT} \qquad (5)$$

Where, A is pre-exponential factor, β is heating rate (20 °C/min), R is general gas constant (8.3143 $Jmol^{-1}K^{-1}$), E_a is activation energy, and T is temperature (Kelvin). Plotting graph between ln[ln(1-x)] vs. 1000/T for each phase (Figure 14) gives the value of activation energy from slope. Further parameters are determined using basic thermodynamic equations shown in Equations (6-8). Values obtained for each phase proved that all phases are non-spontaneous endothermic reactions.

$$E_a = slope * R \qquad (6)$$

$$\Delta S = R\ ln\ ln\ \frac{Ah}{KT} \qquad (7)$$

$$\Delta H = E_a - RT \qquad (8)$$

$$\Delta G = \Delta H - T\Delta S \qquad (9)$$

X-ray diffraction

X-ray diffraction was carried out for the complexes powders of $[Fe(AAN)(H_2O)_2]$, $[Fe(ACl)(H_2O)_2]$, $[Ni(AAN)]$, and $[Co(AAN)(H_2O)_2]$. Their XRD patterns are within the range $10 < 2\theta < 80^o$ and are shown in Figures 21, 22, and 23, respectively. The XRD measurements proved that all the complexes were crystallite as they gave sharp peaks. Sherrer's equation (Equation 1) was used to calculate the average crystal size [17,18]. Scherer's equation is related to the diffraction peak presented in Equation (1), where L is the size of the nanocrystal, K is the shape factor, which is typically taken as 0.89 for ceramic materials, λ is the wavelength of radiation in nanometers (λ = 0.15406 nm), θ is the diffracted angle of the peak, and β is the full width at half maximum of the peak in radians. In addition, physical broadening and instrumental broadening are connected to peak broadening.

$$L = \frac{K\lambda}{\beta\ coscos\ \theta} \qquad (1)$$

Scherer's equation only considers the impact of crystallite size on X-ray diffraction peak broadening. It does not take into account the inherent strain that develops in nanocrystals due to point defects, grain boundaries, triple junctions, and stacking faults. Williamson Hall (W-H) approach (Equation 2), which also calculates the crystal size and the intrinsic strain, is one of the methods taking the effect of strain-induced XRD peak broadening into account. The physical line broadening of the X-ray diffraction peak indicates that it is a result of both size and strain [15,16]. The W-H approach changes with tan in strain considerations rather than confirming a

1/cos dependency as in the Scherer's equation. This fundamental difference combines small crystallite size and microstrain to pursue a dissociation of broadening reflection. This equation provides the distinct correlations of the impacts of size and strain broadening in W-H analysis [16].

$$\beta \ cos\, cos\, \theta = \frac{K\lambda}{L} + 4\,\varepsilon \ sin\, sin\, \theta \qquad (2)$$

When Plotting θ (x-axis) versus $\beta \ cos\, cos\, \theta$ (y-axis), a straight line is gotten with a slope of ε and intercept of $\frac{K\lambda}{L}$ (Figures 21-26). The largest peaks are observed at around 35.3417 °, 23.4078 °, and 10.0866 ° for $[Fe(AAN)(H_2O)_2]$, $[Fe(ACl)(H_2O)_2]$, and $[Ni(AAN)]$, respectively. The crystal size is calculated from Scherrer and Williamson-Hall (Figures 15-20) methods. The strain ε is calculated from Williamson-Hall method. The crystallite sizes obtained from Scherer's equation are 219.19 nm, 125.568 nm, and 4112.53 nm for $[Fe(AAN)(H_2O)_2]$, $[Fe(ACl)(H_2O)_2]$, and $[Ni(AAN)]$, respectively. While those obtained from Williamson-Hall method are 277.3 nm, 143.03 nm, and 3466.35 nm, respectively (Table 3). The differences among crystallite sizes obtained by both methods indicate that the instrumental broadening is less large than that caused by the physical broadening. The presence of chlorine atom in the complex $[Fe(ACl)(H_2O)_2]$ compared with the analogous complex $[Fe(AAN)(H_2O)_2]$ decreased the crystallite size. The strain ε values are $9 * 10^{-5}$, $2 * 10^{-4}$, and $4 * 10^{-6}$, respectively [18,19].

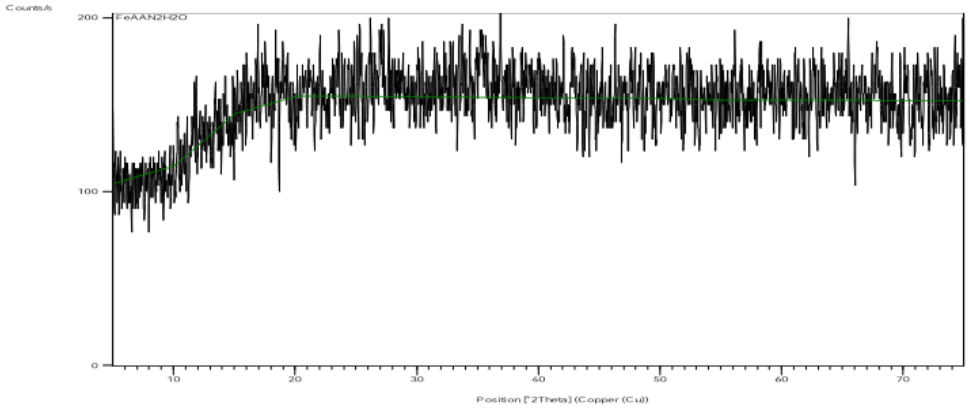

FIGURE 15 XRD pattern of $[Fe(AAN)(H_2O)_2]$

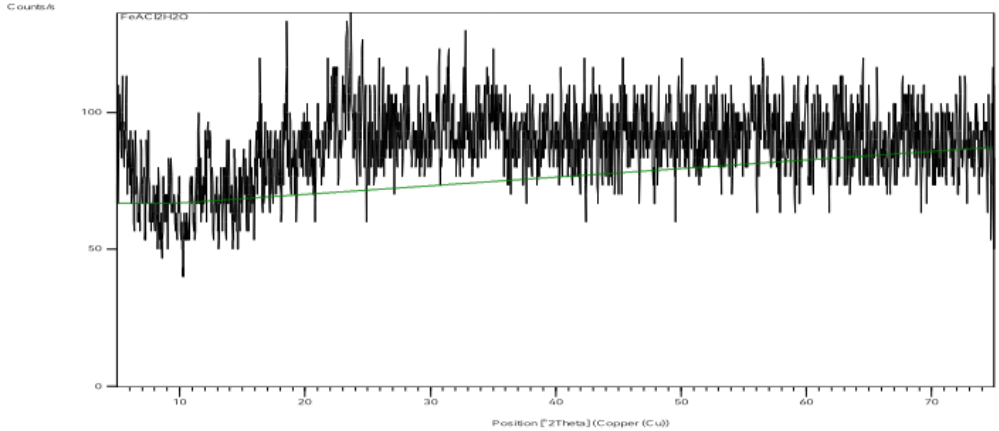

FIGURE 16 XRD pattern of $[Fe(ACl)(H_2O)_2]$

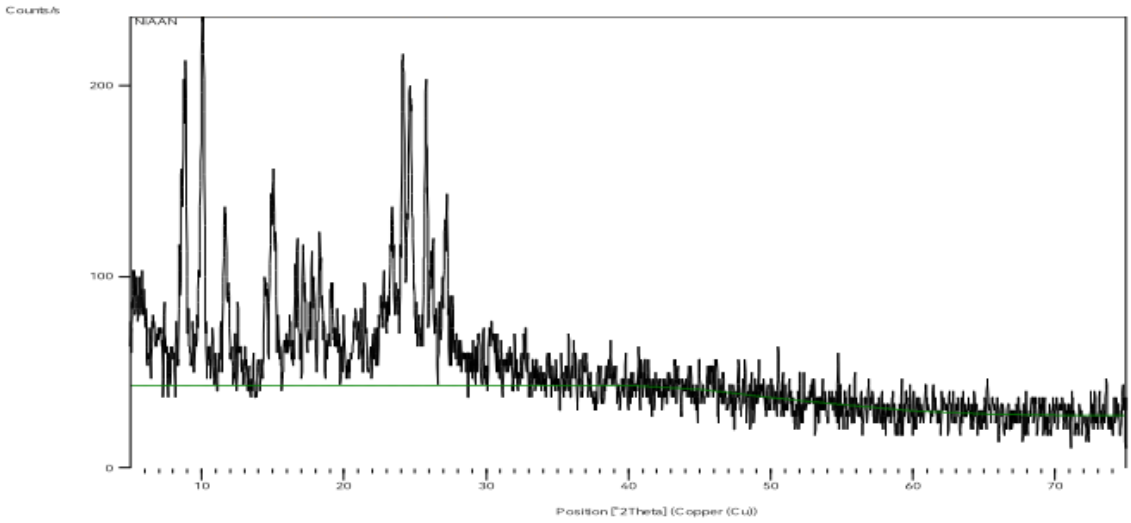

FIGURE 17 XRD pattern of $[Ni(AAN)]$

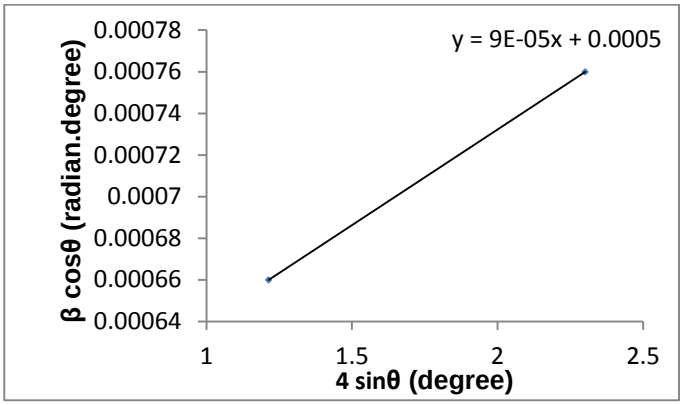

FIGURE 18 Williamson-Hall plot of the complex $[Fe(AAN)(H_2O)_2]$

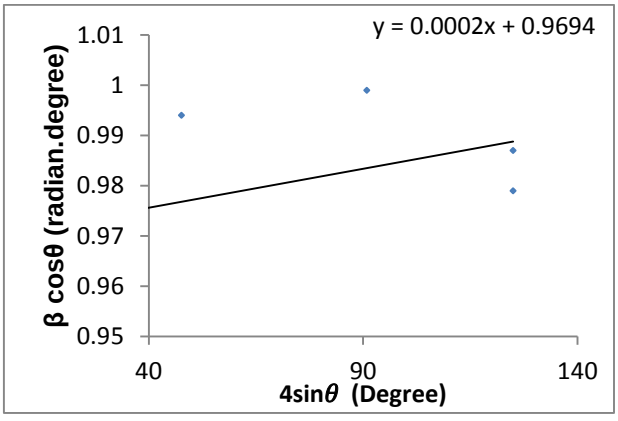

FIGURE 19 Williamson-Hall plot of the complex $[Fe(ACl)(H_2O)_2]$

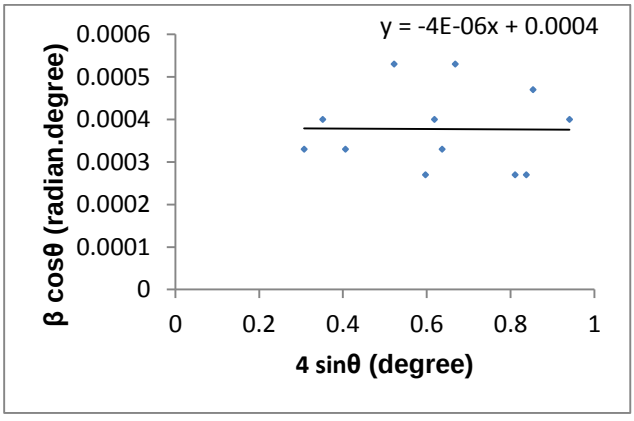

FIGURE 20 Williamson-Hall plot of the complex $[Ni(AAN)]$

TABLE 3 Crystal size and strain of complexes from Scherer's and Williamson-Hall's equations

Complexes	Crystal size L		ε(Strain)
	Scherrer equation	Williamson-Hall equation	
$[Fe(AAN)(H_2O)_2]$.	219.19	277.3	0.00009
$[Fe(ACl)(H_2O)_2]$.	125.568	143.03	0.0002
[Ni(AAN)]	4112.53	3466.35	0.000004

UV-Visible absorption spectroscopy of complexes in different solvents

UV-Visible absorption spectra of the complexes: $[Fe(AAN)(H_2O)_2]$, $[Fe(ACl)(H_2O)_2]$, $[Fe(AAN)(bpy)_2]$, $[Co(AAN)(H_2O)_2]$, and [Ni(AAN)] are recorded in different solvents and at different concentrations. These absorption spectra are depicted in Figure 21. The absorption data of these spectra are listed in Table 4.

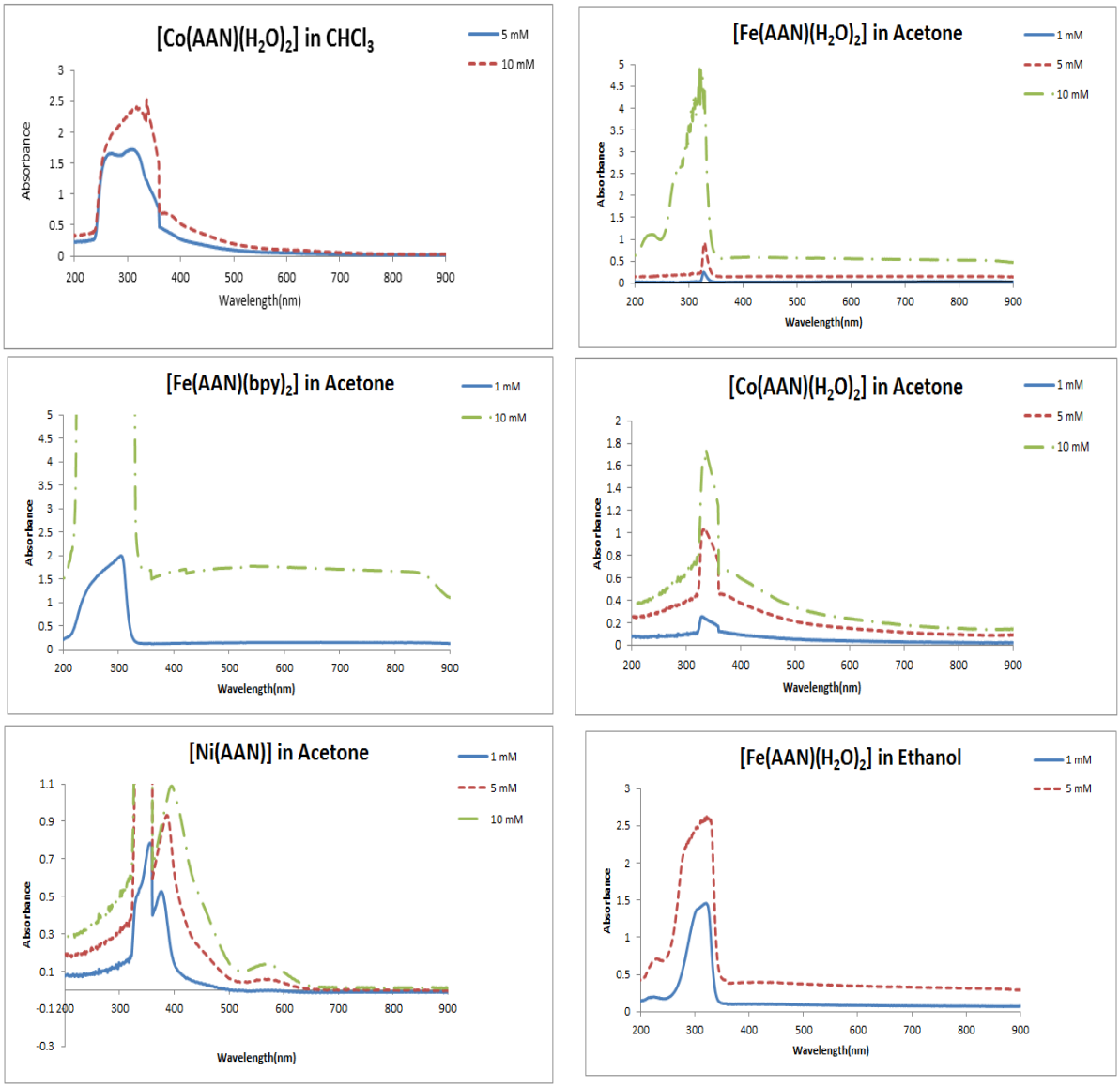

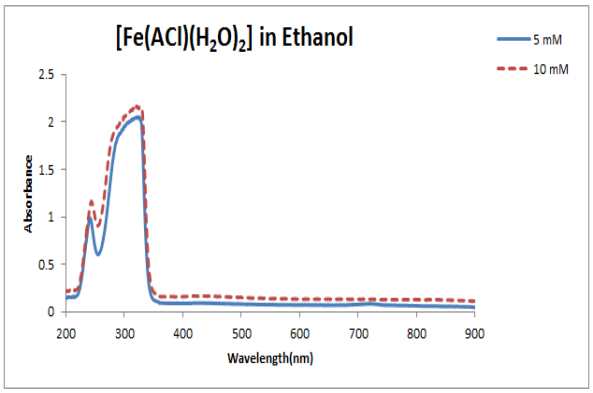
[Fe(ACl)(H2O)2] in Ethanol
5 mM
10 mM
Absorbance
Wavelength(nm)

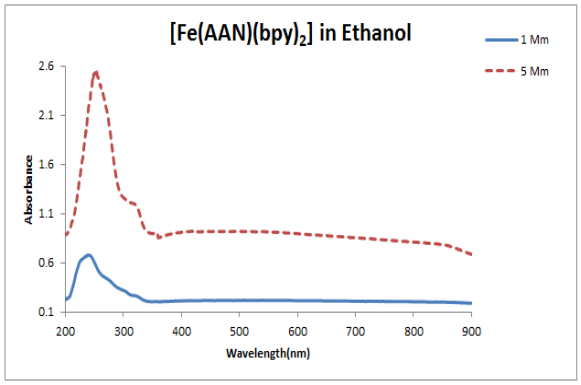
[Fe(AAN)(bpy)2] in Ethanol
1 Mm
5 Mm
Absorbance
Wavelength(nm)

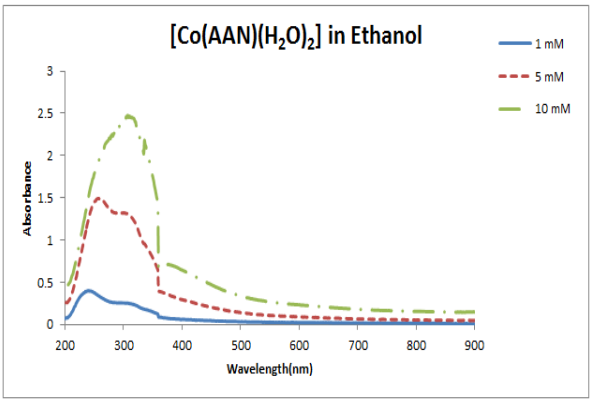
[Co(AAN)(H2O)2] in Ethanol
1 mM
5 mM
10 mM
Absorbance
Wavelength(nm)

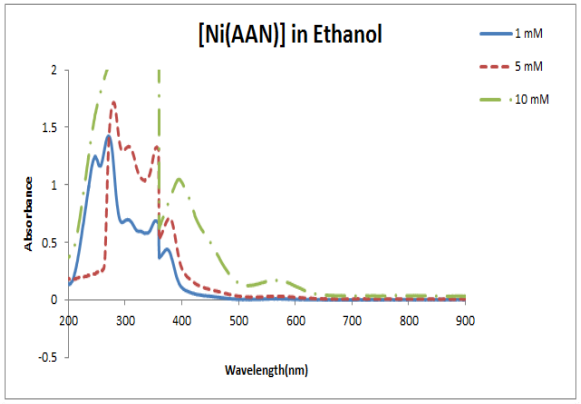
[Ni(AAN)] in Ethanol
1 mM
5 mM
10 mM
Absorbance
Wavelength(nm)

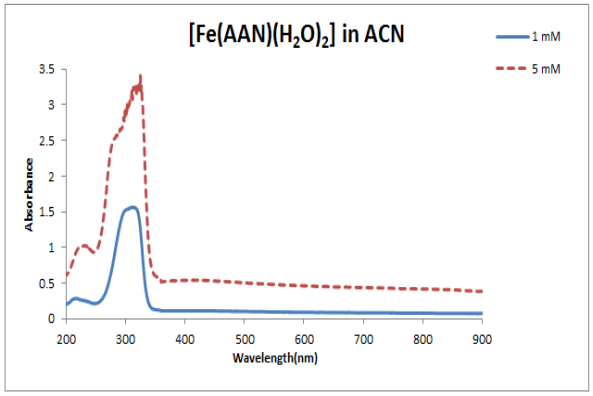
[Fe(AAN)(H2O)2] in ACN
1 mM
5 mM
Absorbance
Wavelength(nm)

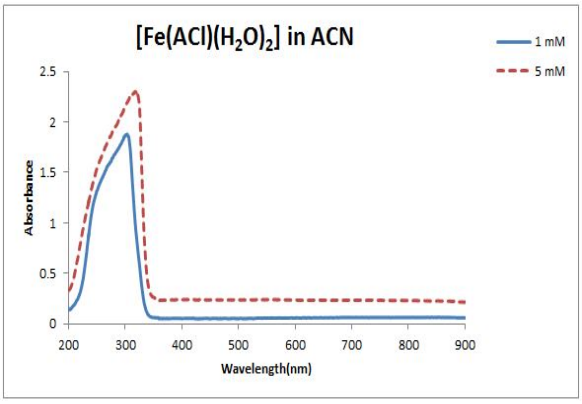
[Fe(ACl)(H2O)2] in ACN
1 mM
5 mM
Absorbance
Wavelength(nm)

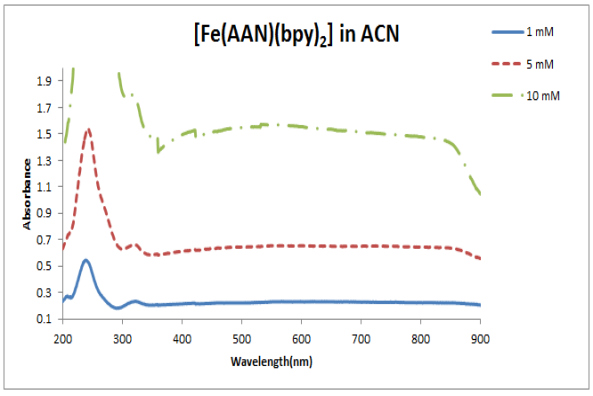
[Fe(AAN)(bpy)2] in ACN
1 mM
5 mM
10 mM
Absorbance
Wavelength(nm)

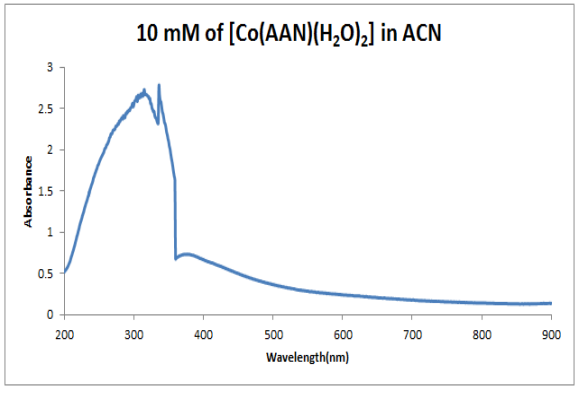
10 mM of [Co(AAN)(H2O)2] in ACN
Absorbance
Wavelength(nm)

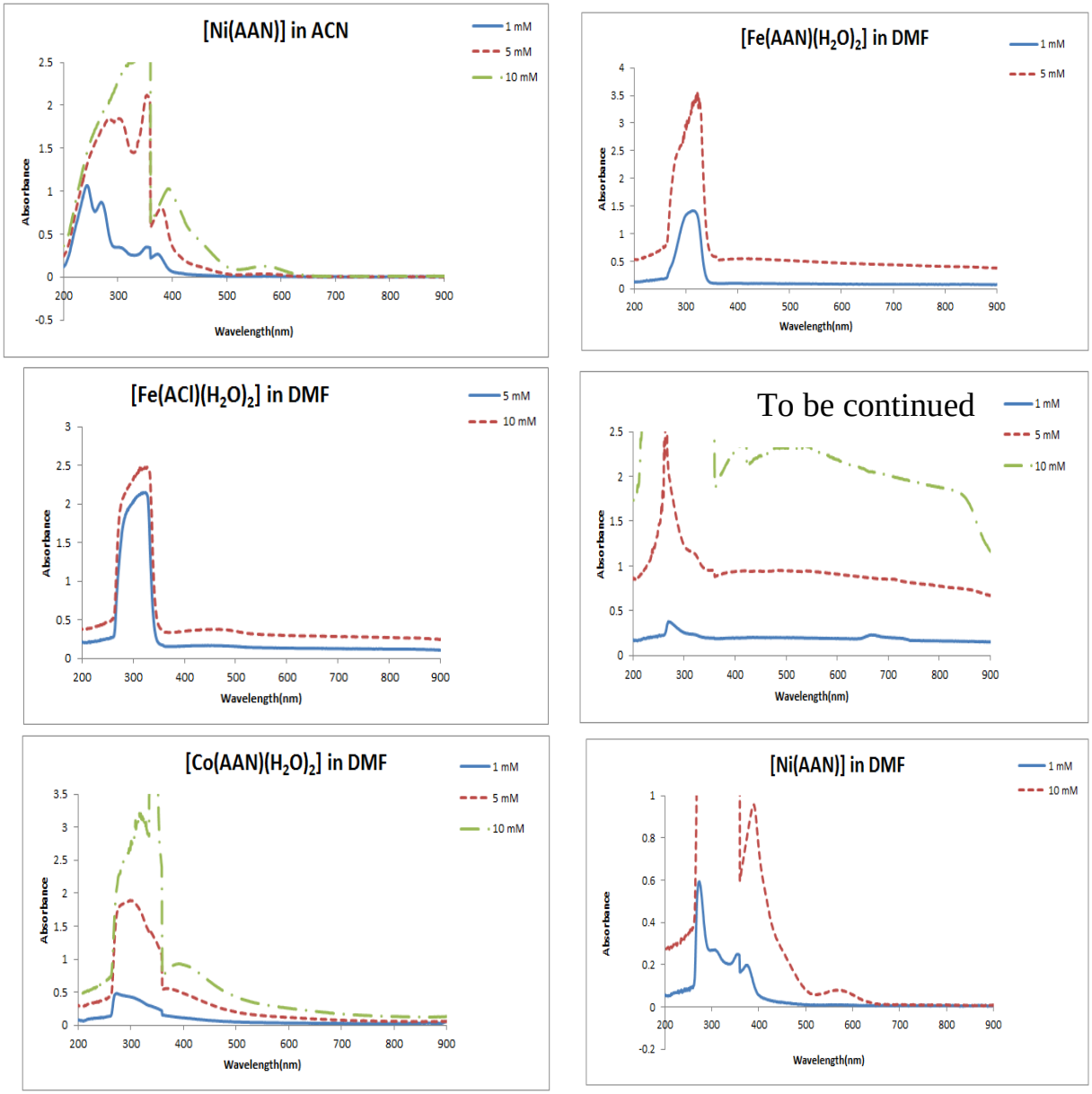

FIGURE 21 UV-Visible absorption spectra of the complexes: $[Co(AAN)(H_2O)_2]$, $[Fe(AAN)(H_2O)_2]$, $[Fe(ACl)(H_2O)_2]$, $[Fe(AAN)(bpy)_2]$, and [Ni(AAN)] in different solvents.

TABLE 4 UV-Visible absorption data of different concentrations of the complexes: $[Co(AAN)(H_2O)_2]$, $[Fe(AAN)(H_2O)_2]$, $[Fe(ACl)(H_2O)_2]$, $[Fe(AAN)(bpy)_2]$, and [Ni(AAN)] in different solvents.

Complex	Concentration (M)	λ_{max} /nm (ε /L.mol^{-1}.cm^{-1})	Solvent
$[Co(AAN)(H_2O)_2]$	5 mM	257(310), 309(345), 388(70)	$CHCl_3$
	10 mM	317(240), 336(250), 375(70)	
$[Fe(AAN)(H_2O)_2]$	1 mM	327(250)	Acetone
	5 mM	329(185)	
	10 mM	226(110), 275(245), 320(490)	
$[Fe(AAN)(bpy)_2]$	1 mM	260(1540), 308(1935)	Acetone
	10 mM	857(155)	
$[Co(AAN)(H_2O)_2]$	1 mM	328(250), 368(120)	Acetone
	5 mM	325(125), 388(80)	
	10 mM	336(175), 375(65), 390(45)	

[Ni(AAN)]	1 mM	335(525), 359(770), 377(525)	Acetone
	5 mM	389(185), 581(10)	
	10 mM	394(110), 583(15)	
[Fe(AAN)(H₂O)₂]	1 mM	219(200), 304(1375), 323(1440)	Ethanol
	5 mM	228(140), 319(520), 427(80)	
[Fe(ACl)(H₂O)₂]	5 mM	244(190), 296(380), 329(400)	Ethanol
	10 mM	248(105), 287(195), 331(210), 450(20)	
[Fe(AAN)(bpy)₂]	1 mM	232(650), 242(675),279(410), 308(290), 322(265)	Ethanol
	5 mM	252(510), 321(240), 359(180)	
[Co(AAN)(H₂O)₂]	1 mM	254(360), 321(230), 370(80)	Ethanol
	5 mM	270(285), 319(245), 372(75)	
	10 mM	321(240), 340(205), 393(65), 453(45)	
[Ni(AAN)]	1 mM	248(1245), 272(1420), 304(700), 354(685), 375(435)	Ethanol
	5 mM	280(345), 306(265), 356(265), 379(140), 578(5)	
	10 mM	394(105), 581(15)	
[Fe(AAN)(H₂O)₂]	1 mM	217(285), 297(1495), 310(1560)	ACN
	5 mM	226(205), 283(505), 325(680), 358(115), 422(110)	
[Fe(ACl)(H₂O)₂]	5 mM	252(270), 307(365)	ACN
	10 mM	254(160), 323(225)	
[Fe(AAN)(bpy)₂]	1 mM	208(275), 237(540), 322(235)	ACN
	5 mM	246(300), 329(125)	
	10 mM	324(175), 421(155), 849(145)	
[Co(AAN)(H₂O)₂]	10 mM	315(275), 336(275), 380(75)	ACN
[Ni(AAN)]	1 mM	246(1040), 274(820), 314(305), 359(340), 379(235)	ACN
	5 mM	284(370), 304(370), 352(420), 379(160), 567(10)	
	10 mM	394(105), 581(10)	
[Fe(AAN)(H₂O)₂]	1 mM	305(1380), 321(1360)	DMF
	5 mM	228(120), 322(710), 359(115), 437(110)	
[Fe(ACl)(H₂O)₂]	5 mM	292(390), 328(420), 487(35)	DMF
	10 mM	285(215), 331(245), 482(35)	
[Fe(AAN)(bpy)₂]	1 Mm	269(380), 327(225), 667(230), 735(185)	DMF
	5 mM	266(65), 325(220), 398(185), 719(170)	
	10 mM	422(240), 545(235), 853(175)	
[Co(AAN)(H₂O)₂]	1 mM	265(235), 341(285), 371(145)	DMF
	5 mM	284(365),313(360), 390(105)	
	10 mM	240(460),325(310), 352(355), 411(90)	
[Ni(AAN)]	1 mM	276(575), 315(250), 359(245), 380(185)	DMF
	10 mM	393(90), 578(10)	

The solution of 5 mM $[Co(AAN)(H_2O)_2]$ in $CHCl_3$ absorbed at 257 nm, 309 nm, and 388 nm. These bands are attributed to $\pi - \pi^*$ transition or/and $\pi - \pi^*$ transition merged with $n - \pi^*$ transition. The absorption at 257 nm in $CHCl_3$ is red shifted to 270 nm and 284 nm in ethanol and DMF, respectively. The orbital π^* is more polar than π orbital. Then, the orbital π^* is more affected by polar solvent than π orbital. A more lowering in energy of π^* orbital is more polar solvent than the energy of π orbital. Hence, lower energy is required for $\pi - \pi^*$ transition at the more polar solvent. Therefore, red shift in

$\pi - \pi^*$ transition happened at more polar solvents. For $n - \pi^*$ transition, the n orbital is much polar orbital than π^* orbital. Then, n orbital will more interact with polar solvent than π^* orbital. This will much decrease n orbital energy than π^* orbital energy. Therefore, at moving to more polar solvent, more energy is required to get $n - \pi^*$ transition. In other words, blue shift happens for $n - \pi^*$ transition in a more polar solvent. If the $\pi - \pi^*$ transition is merged with $n - \pi^*$ transition, then a net effect of both the red and blue shifts should be noted. The transition at 309 nm in $CHCl_3$ is shifted to 325 nm, 319 nm, and 313 nm in acetone, ethanol, and DMF, respectively. The band at 388 nm in $CHCl_3$ is noted at 388 nm, 372 nm, and 390 nm in acetone, ethanol, and DMF, respectively. For all complexes, it is noted that fine structures of their spectra are disappeared gradually with increasing concentrations. The absorption intensities of complexes increase with increasing their concentration according to Lambert Beer's law. Also, remarkable shifts in the absorptions are noted with increasing the complexes concentrations. These shifts could be correlated with decrease of solvent - solute interactions at increase of solute concentrations. Same trends are noted for the other complexes. The transition band occurred at 427 nm for the spectrum of $[Fe(AAN)(H_2O)_2]$ in ethanol could be attributed to $d - d$ transition. This band is red shifted to 450 nm for the complex $[Fe(ACl)(H_2O)_2]$. This shift refers that the ligand AAN is stronger than ACl. Likewise, the same red shift was noted for both complexes in DMF. Thus, $d - d$ transitions occurred at 437 nm and 487 nm in DMF for $[Fe(AAN)(H_2O)_2]$ and $[Fe(ACl)(H_2O)_2]$, respectively [20,21]. The reaction of $[Fe(AAN)(H_2O)_2]$ with 5 equivalents of $4,4' -$ *bipyridine* at lab temperature afforded the complex $[Fe(AAN)(bpy)_2]$. Dramatic absorption changes are noted between $[Fe(AAN)(bpy)_2]$ and its precursor $[Fe(AAN)(H_2O)_2]$ in both UV and visible regions. For example, $d - d$ transitions of $[Fe(AAN)(bpy)_2]$ occurred at lower energies 857 nm, 849 nm, and 667 nm in acetone, acetonitrile, and DMF, respectively. The square planer complex [Ni(AAN)] showed perfectly the expected broad $d - d$ transition band at 583 nm, 581 nm, and 578 nm in acetone, ethanol, acetonitrile, and DMF, respectively [22,23].

Interaction of the complexes with bpy (formation of adducts)

The interaction of the complexes $[Fe(AAN)(H_2O)_2]$, $[Fe(ACl)(H_2O)_2]$, $[Co(AAN)(H_2O)_2]$, and [Ni(AAN)] with $4,4' -$ *bipyridine* affording the adduct complexes is followed by UV-Visible absorption spectroscopy. These absorption spectra and their data are shown in Figures 22-25 and Table 5, respectively. The proposed adduct complexes resulted from those mentioned interactions are shown in Scheme 5.

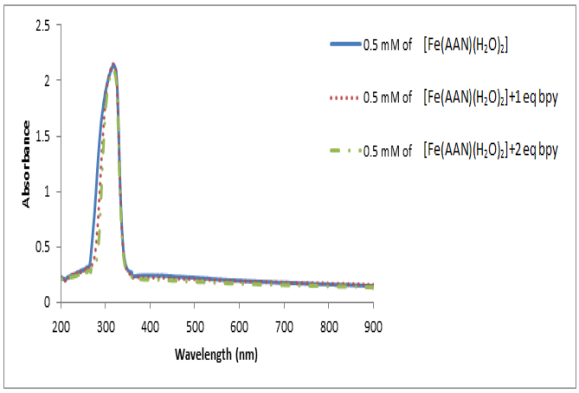

FIGURE 22 UV-Visible absorption spectra of 0.5

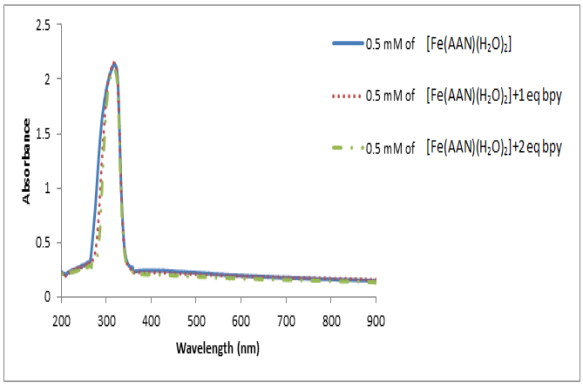

FIGURE 23 UV-Visible absorption spectra of 0.5

mM of $[Fe(AAN)(H_2O)_2]$ (solid blue line), its mixture with 1 eq (red dotted line) and 2 eq (green dash line) of bpy in DMF at r.t using quartz cell with a path length of 1 cm.

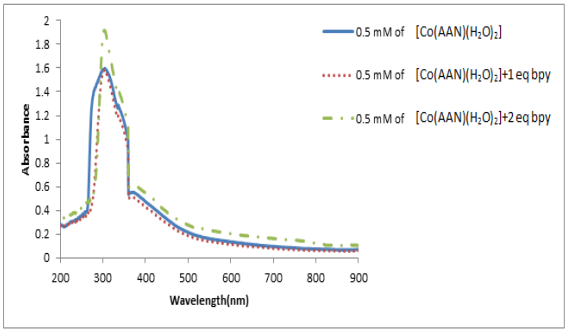

FIGURE 24 UV-Visible absorption spectra of 0.5 mM of $[Co(AAN)(H_2O)_2]$ (solid blue line), its mixture with 1 eq (red dotted line) and 2 eq (green dash line) of bpy in DMF at r.t using quartz cell with a path length of 1 cm.

mM of $[Fe(ACl)(H_2O)_2]$ (solid blue line), its mixture with 1 eq (red dotted line) and 2 eq (green dash line) of bpy in DMF at r.t using quartz cell with a path length of 1 cm

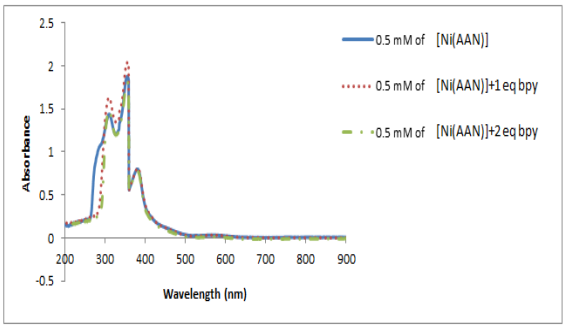

FIGURE 25 UV-Visible absorption spectra of 0.5 mM of [Ni(AAN)] (solid blue line), its mixture with 1 eq (red dotted line) and 2 eq (green dash line) of bpy in DMF at r.t using quartz cell with a path length of 1 cm

TABLE 5 UV-Visible absorption data of 0.5 mM of each of $[Co(AAN)(H_2O)_2]$, $[Fe(AAN)(H_2O)_2]$, $[Fe(ACl)(H_2O)_2]$, and [Ni(AAN)] and their mixtures with 1eq and 2eq bpy in DMF at r.t using quartz cell with path length of 1 cm

Complex	λ_{max} /nm (ε /L.mol^{-1}.cm^{-1})
0.5 mM of $[Fe(AAN)(H_2O)_2]$	320(4260)
0.5 mM of $[Fe(AAN)(H_2O)_2]$ with 1eq bpy	320(4265)
0.5 mM of $[Fe(AAN)(H_2O)_2]$ with 2eq bpy	320(4165)
0.5 mM of $[Fe(ACl)(H_2O)_2]$	300(2085), 390(780), 457(760)
0.5 mM of $[Fe(ACl)(H_2O)_2]$ with 1eq bpy	296(1950), 390(625), 464(520)
0.5 mM of $[Fe(ACl)(H_2O)_2]$ with 2eq bpy	307(1635), 390(575), 468(610)
0.5 mM of $[Co(AAN)(H_2O)_2]$	287(2915), 315(3070), 359(1990), 387(1080)
0.5 mM of $[Co(AAN)(H_2O)_2]$ with 1eq bpy	310(3065), 391(915)
0.5 mM of $[Co(AAN)(H_2O)_2]$ with 2eq bpy	308(3745), 391(1145), 552(460)
0.5 mM of [Ni(AAN)]	293(2225), 315(2785), 359(3680), 386(1505), 580(60)
0.5 mM of [Ni(AAN)] with 1eq bpy	315(3145), 359(4010), 386(1555), 580(60)
0.5 mM of [Ni(AAN)] with 2eq bpy	315(2850), 359(3555), 386(1460), 577(20)

The UV-Visible spectrum of 0.5 mM $[Fe(AAN)(H_2O)_2]$ showed intense peak at 320 nm. After addition of 1 or 2 equivalent of $4,4' - bipyridine$, intensity of this absorption changed that could be correlated with displacement of one (more possible) or two water molecules by one or two bipyridine molecules, respectively, and formation of the adduct (Figure 28 and Scheme 5). The complex $[Fe(ACl)(H_2O)_2]$ showed absorptions at 300 nm, 390 nm, and 457 nm. After addition of 1 equivalent to the complex solution, those mentioned absorptions are noted at 296 (blue shifted and lower intensity), 390 nm (Same with lower intensity), and 464 nm (red shifted with lower intensity). At comparison with the free complex, red shift with lower intensity (307 nm), the same with lower intensity (390 nm) and red shift with lower intensity (610 nm) are seen after addition of 2 equivalents of bipyridine. These changes in both the maximum wavelength and intensities are due to coordination of bipyridine with Fe^{2+} ion

instead of water molecule and formation of the adduct complex. The noted changes after addition of 2 equivalents of bipyridine compared with the case of 1 equivalent of bipyridine could be attributed to coordination of two bpy moieties with the free complex and formation of $[Fe(ACl)(bpy)_2]$. The absorptions of $[Co(AAN)(H_2O)_2]$ (Figure 24) occurred at 287 nm, 315 mm, 359 nm and 387 nm are disappeared blue shifted (310 nm), blue shifted (with lower intensity), and red shifted (391 nm with lower intensity) after mixing with 1 equivalent of bipyridine. Important changes are also happened after addition of 2 equivalents of bipyridine to the free complex solution. These big changes are undoubtedly assigned to the formation of the adduct complexes: $[Co(AAN)(bpy)(H_2O)]$ or also probably the $[Co(AAN)(bpy)_2]$ after adding 1 or 2 equivalents of bpy, respectively. The complex [Ni(AAN)] absorbed at 293 nm, 315 nm, 359 nm, 386 nm, and 580 nm. After addition of 1 equivalent of bpy, these absorptions are disappeared, decreased in intensity, increased in intensity, increased in intensity, and at same intensity respectively. Changes in intensity and blue shift (with lower intensity) for the last peak are noted after mixing with 2 equivalent of bpy moiety. These changes are due to formation of the adduct complex: [Ni(AAN)(bpy)] and $[Ni(AAN)(bpy)_2]$ or larger amounts bpy of [Ni(AAN) bpy] after mixing with 1 and 2 equivalents of bpy moieties respectively [23,24].

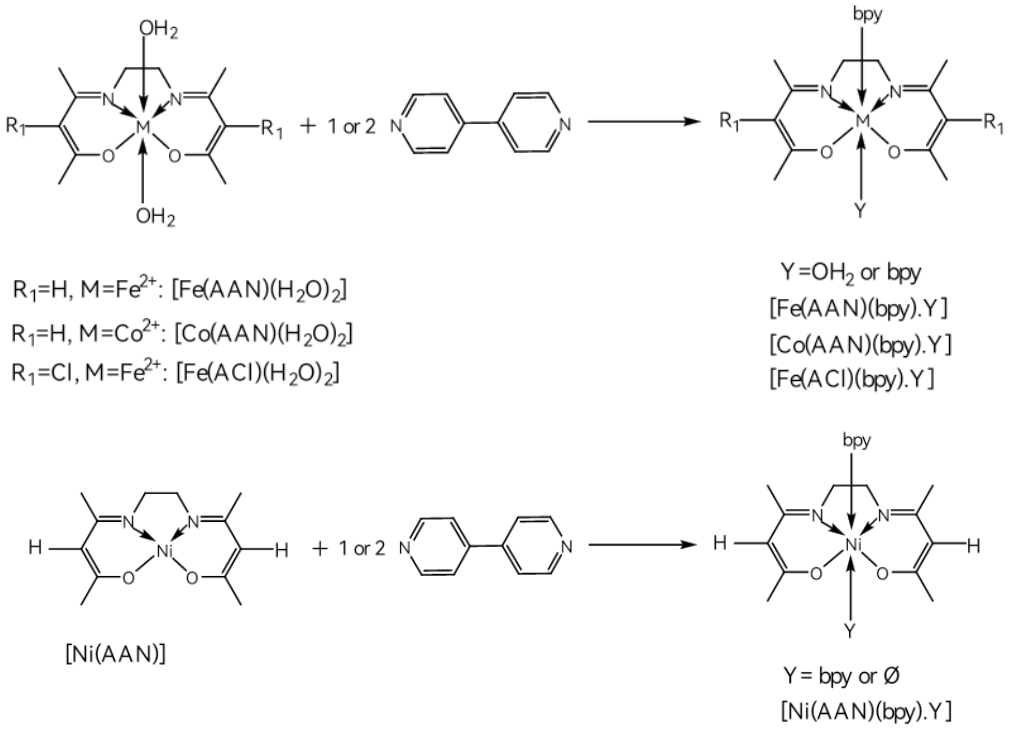

SCHEME 5 Formation of adduct complexes: [M(AAN)(bpy).Y] (M^{2+}=Fe^{2+} or Co^{2+}), [Fe(ACl)(bpy).Y], and [Ni(AAN)(bpy).Y], Y= OH_2, bpy or Ø

Interaction of the complexes with $V_2^{2+}.2PF_6^-$ (formation of adducts)

The reaction of complexes $[Fe(AAN)(H_2O)_2]$, $[Fe(ACl)(H_2O)_2]$, $[Co(AAN)(H_2O)_2]$, and [Ni(AAN)] with 1 or 2 equivalents of $V_2^{2+}.2PF_6^-$ are performed in DMF at lab temperature and followed by UV-Visible absorption spectroscopy. The absorption spectra of those reaction mixtures are depicted in Figures 26-29. Their data are listed in Table 6.

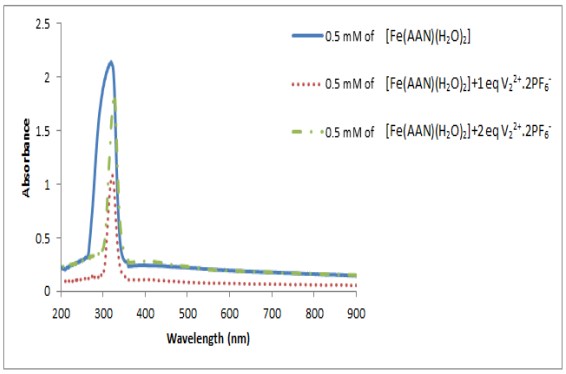

FIGURE 26 UV-Visible absorption spectra of 0.5 mM $[Fe(AAN)(H_2O)_2]$ (solid blue line), its mixture with 1 eq (red dotted line), and 2 eq (green dash line) of $V_2^{2+}.2PF_6^-$ in DMF at r.t using quartz cell with a path length of 1 cm.

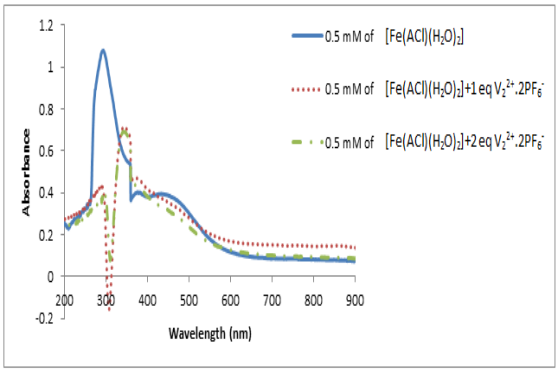

FIGURE 27 UV-Visible absorption spectra of 0.5 mM $[Fe(ACl)(H_2O)_2]$ (solid blue line), its mixture with 1 eq (red dotted line), and 2 eq (green dash line) of $V_2^{2+}.2PF_6^-$ in DMF at r.t using quartz cell with a path length of 1 cm.

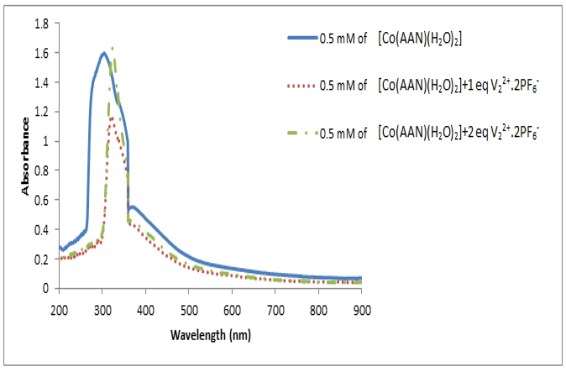

FIGURE 28 UV-Visible absorption spectra of 0.5 mM $[Co(AAN)(H_2O)_2]$ (solid blue line), its mixture with 1 eq (red dotted line), and 2 eq (green dash line) of $V_2^{2+}.2PF_6^-$ in DMF at r.t using quartz cell with a path length of 1 cm.

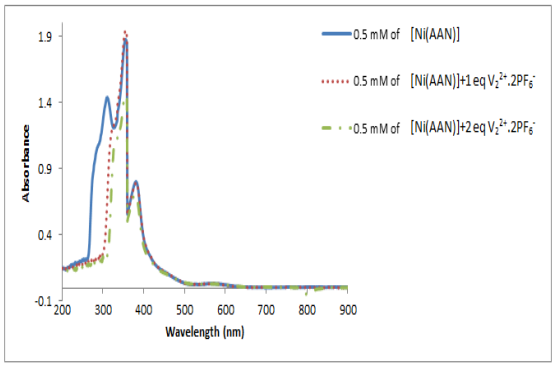

FIGURE 29 UV-Visible absorption spectra of 0.5 mM [Ni(AAN)] (solid blue line), its mixture with 1 eq (red dotted line), and 2 eq (green dash line) of $V_2^{2+}.2PF_6^-$ in DMF at r.t using quartz cell with a path length of 1 cm.

TABLE 6 UV-Visible absorption data of 0.5 mM of each of $[Co(AAN)(H_2O)_2]$, $[Fe(AAN)(H_2O)_2]$, $[Fe(ACl)(H_2O)_2]$, and [Ni(AAN)] and their mixtures with $V_2^{2+}.2PF_6^-$ in DMF at r.t using quartz cell with a path length of 1cm.

Complex	λ_{max} /nm (ε /L.mol^{-1}.cm^{-1})
0.5 mM $[Fe(AAN)(H_2O)_2]$	320(4260), 426(485)
0.5 mM $[Fe(AAN)(H_2O)_2]$ + 1eq $V_2^{2+}.2PF_6^-$	324(2090), 439(200)
0.5 mM $[Fe(AAN)(H_2O)_2]$ + 2eq $V_2^{2+}.2PF_6^-$	324(3635), 421(555)
0.5 mM $[Fe(ACl)(H_2O)_2]$	300(2085), 390(780), 461(755)
0.5 mM $[Fe(ACl)(H_2O)_2]$ + 1eq $V_2^{2+}.2PF_6^-$	300(340), 353(1380), 390(880)
0.5 mM $[Fe(ACl)(H_2O)_2]$ + 2eq $V_2^{2+}.2PF_6^-$	300(795), 353(1330), 390(810)
0.5 mM $[Co(AAN)(H_2O)_2]$	284(2905), 313(3100), 386(1035), 349(1965)
0.5 mM $[Co(AAN)(H_2O)_2]$ + 1eq $V_2^{2+}.2PF_6^-$	326(2260), 357(1555), 386(780)
0.5 mM $[Co(AAN)(H_2O)_2]$ + 2eq $V_2^{2+}.2PF_6^-$	327(3190), 359(1615), 386(845)
0.5 mM [Ni(AAN)]	285(2090), 316(2750), 359(3680), 386(1505), 583(60)
0.5 mM [Ni(AAN)] + 1eq $V_2^{2+}.2PF_6^-$	323(2395), 359(3780), 386(1500), 583(60)
0.5 mM [Ni(AAN)] + 2eq $V_2^{2+}.2PF_6^-$	344(2455), 359(2840), 386(1260), 583(55)

The 0.5 mM $[Fe(AAN)(H_2O)_2]$ absorbed at 324 nm and 426 nm. These absorptions are noted at 324 nm (with lower intensity) and 439 nm (with lower intensity), respectively, in the mixture of $[Fe(AAN)(H_2O)_2]$ with 1 equivalent of $V_2^{2+}.2PF_6^-$. At mixing with 2 equivalents of $V_2^{2+}.2PF_6^-$, the absorptions happened at 324 nm (with lower intensity) and 421 mm (with higher intensity), respectively. The complex $[Fe(ACl)(H_2O)_2]$ showed the absorptions 300 nm, 390 nm, and 461 nm. The mixture of $[Fe(ACl)(H_2O)_2]$ with 1 equivalent of $V_2^{2+}.2PF_6^-$ showed absorptions at 300 nm (with lower intensity), 353 nm (new), 390 nm (with lower intensity), and disappearance of 481 nm, respectively, compared with absorptions of free complex. The same changes are noted for the mixture of free complex with 2 equivalent $V_2^{2+}.2PF_6^-$. The absorptions of $[Co(AAN)(H_2O)_2]$ occurred at 284 nm, 313 nm, 349 nm, and 386 nm are respectively disappeared, red shifted to 326 nm, blue shifted to 357 nm, and noted at the same position with lower intensity in the mixture of $[Co(AAN)(H_2O)_2]$ with 1 equivalent $V_2^{2+}.2PF_6^-$. The same notes are seen in the spectrum of the mixture with 2 equivalents of $V_2^{2+}.2PF_6^-$. The changes in λ_{max} value and intensities of the complexes mixtures with $V_2^{2+}.2PF_6^-$ refer to the formation of their adduct complexes, i.e. complexation of $V_2^{2+}.2PF_6^-$ with Fe^{2+} and Co^{2+} ions. The absorption changes noted here are less than those noted in the case of bipyridine that could be corrected with the lower donor property of $V_2^{2+}.2PF_6^-$ moiety compared with that of bpy moiety. The absorptions of complex [Ni(AAN)] happened at 285 nm, 316 nm, 359 nm, 386 nm, and 583 nm. These absorptions change to be disappeared, at 323 nm (red shift), 359 (with higher intensity), 386 nm (almost same intensity), and 583 nm (same intensity) at mixing the complex [Ni(AAN)] with 1 equivalent of $V_2^{2+}.2PF_6^-$. More changes are noted at mixing with 2 equivalent of $V_2^{2+}.2PF_6^-$. These absorption spectra changes are due to the formation of the adduct complex among [Ni(AAN)] and $V_2^{2+}.2PF_6^-$. The less absorptions changes noted at mixing the complexes with $V_2^{2+}.2PF_6^-$ are undoubtedly due to less coordination strength with $V_2^{2+}.2PF_6^-$ and/or lower adducts quantities have been formed. The proposed adducts complexes are shown in Scheme 6 [25,7].

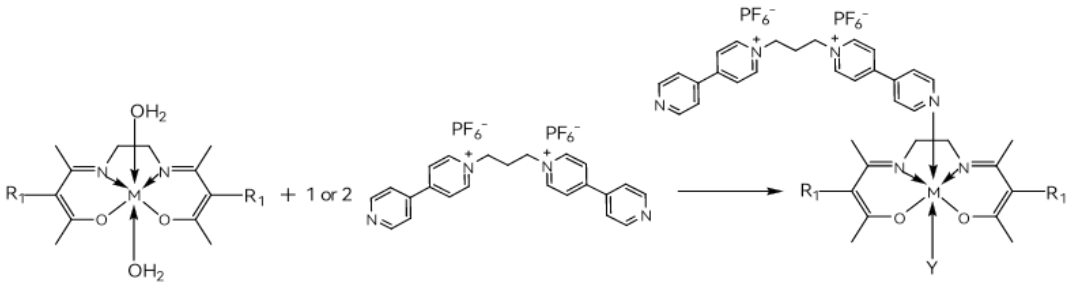

R_1=H, M=Fe^{2+}: $[Fe(AAN)(H_2O)_2]$
R_1=H, M=Co^{2+}: $[Co(AAN)(H_2O)_2]$
R_1=Cl, M=Fe^{2+}: $[Fe(ACl)(H_2O)_2]$

Y=OH_2 or $V_2^{2+}.2PF_6^-$
$[Fe(AAN)(V_2^{2+}.2PF_6^-).Y]$
$[Co(AAN)(V_2^{2+}.2PF_6^-).Y]$
$[Fe(ACl)(V_2^{2+}.2PF_6^-).Y]$

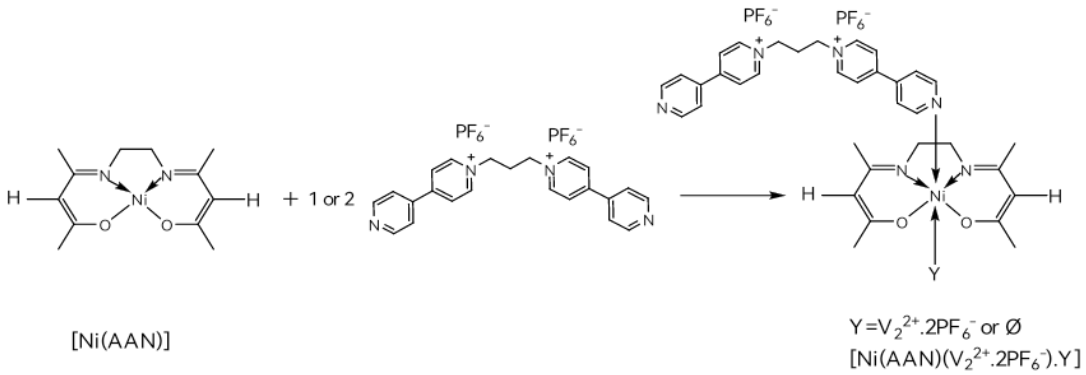

SCHEME 6 Formation of adduct complexes: [M(AAN)($V_2^{2+}.2PF_6^-$).Y] (M^{2+}=Fe^{2+} or Co^{2+}), [Fe(ACl)($V_2^{2+}.2PF_6^-$).Y], [Ni(AAN)($V_2^{2+}.2PF_6^-$).Y], and Y= OH_2, $V_2^{2+}.2PF_6^-$ or Ø.

Reduction of adducts complexes with $V_2^{2+}.2PF_6^-$ *(formation of molecular switches)*

The solutions of adducts complexes formed from the mixtures of complexes and $V_2^{2+}.PF_6^-$ are reduced with activated Zine powder. The UV-Visible absorption spectra are recorded for both adducts complexes solutions and those reduced ones are shown in Figures 30-37. Table 7 contains their absorption data.

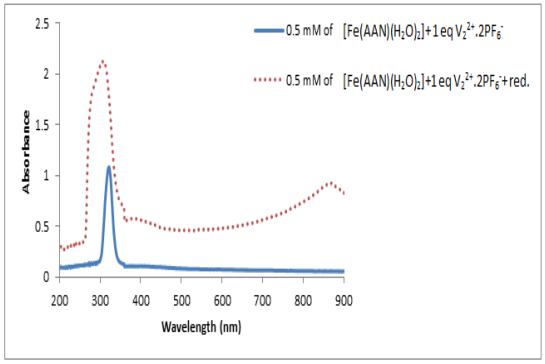

FIGURE 30. UV-Visible absorption spectra of 0.5 mM [Fe(AAN)(H_2O)$_2$] with 1 eq of V_2^{2+} (solid blue line) and its reduced solution by activated zinc powder (dash red line) in DMF at r.t using quartz cell with a path length of 1 cm.

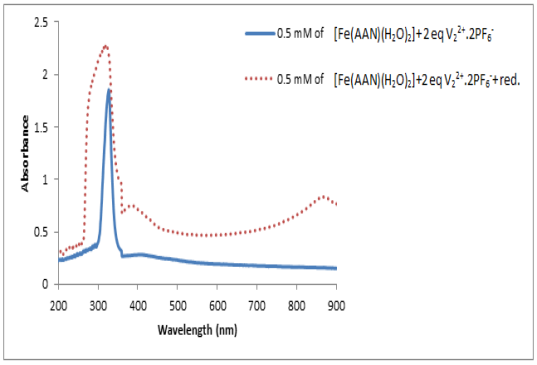

FIGURE 31 UV-Visible absorption spectra of 0.5 mM [Fe(AAN)(H_2O)$_2$] with 2 eq of V_2^{2+} (solid blue line) and its reduced solution by activated zinc powder (dash red line) in DMF at r.t using quartz cell with a path length of 1 cm.

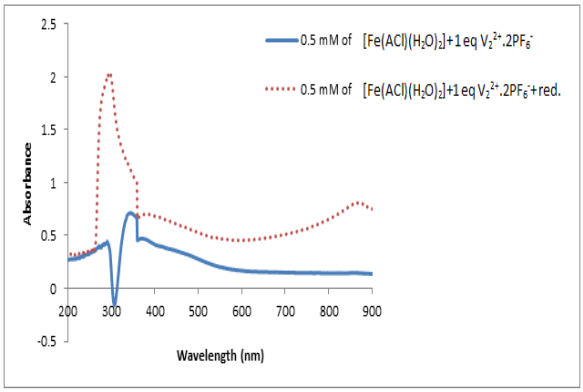

FIGURE 32 UV-Visible absorption spectra of 0.5 mM [Fe(ACl)(H_2O)$_2$] with 1 eq of V_2^{2+} (solid blue line) and its reduced solution by activated zinc powder (dash red line) in DMF at r.t using quartz cell with a path length of 1 cm.

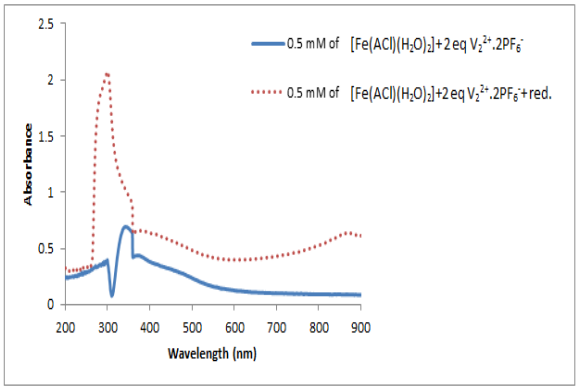

FIGURE 33 UV-Visible absorption spectra of 0.5 mM [Fe(ACl)(H_2O)$_2$] with 2 eq of V_2^{2+} (solid blue line) and its reduced solution by activated zinc powder (dash red line) in DMF at r.t using quartz cell with a path length of 1 cm.

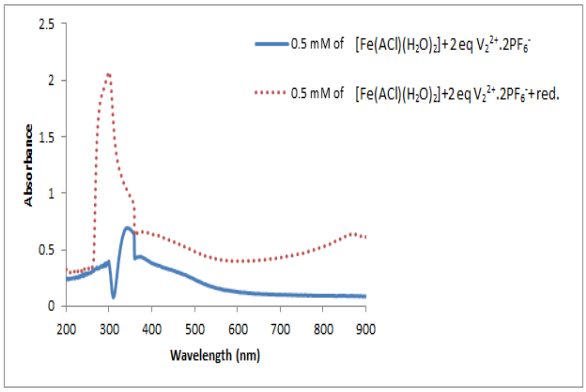

FIGURE 34 UV-Visible absorption spectra of 0.5 mM $[Co(AAN)(H_2O)_2]$ with 1 eq of V_2^{2+} (solid blue line) and its reduced solution by activated zinc powder (dash red line) in DMF at r.t using quartz cell with a path length of 1 cm.

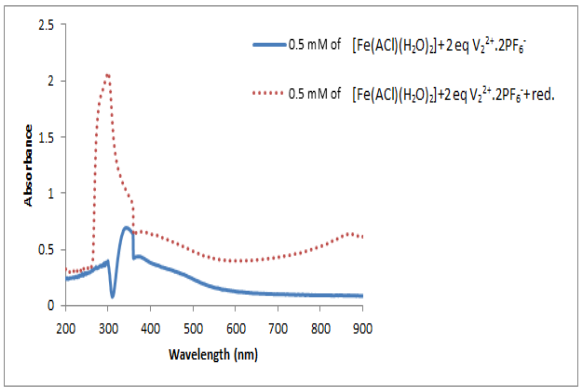

FIGURE 35 UV-Visible absorption spectra of 0.5 mM $[Co(AAN)(H_2O)_2]$ with 2 eq of V_2^{2+} (solid blue line) and its reduced solution by activated zinc powder (dash red line) in DMF at r.t using quartz cell with a path length of 1 cm.

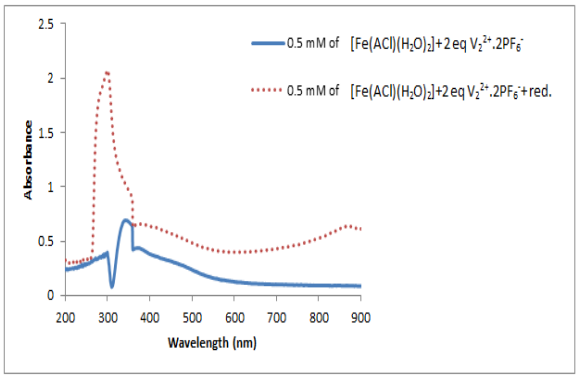

FIGURE 36 UV-Visible absorption spectra of 0.5 mM [Ni(AAN)] with 1 eq of V_2^{2+} (solid blue line) and its reduced solution by activated zinc powder (dash red line) in DMF at r.t using quartz cell with a path length of 1 cm.

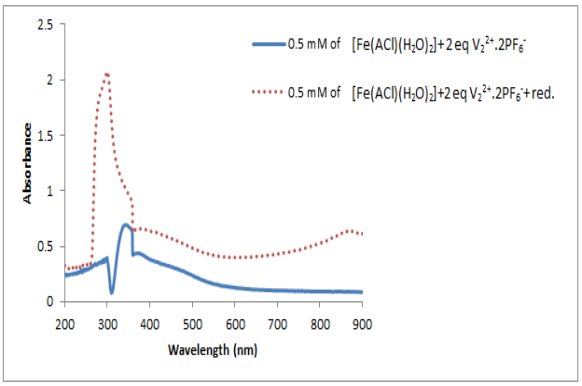

FIGURE 37 UV-Visible absorption spectra of 0.5 mM [Ni(AAN)] with 2 eq of V_2^{2+} (solid blue line) and its reduced solution by activated zinc powder (dash red line) in DMF at r.t using quartz cell with a path length of 1 cm.

TABLE 7 UV-Visible absorption data of 0.5 mM of $[Co(AAN)(H_2O)_2]$, $[Fe(AAN)(H_2O)_2]$, $[Fe(ACl)(H_2O)_2]$, and [Ni(AAN)], their mixtures with V_2^{2+} and their reduced solutions by activated zinc powder in DMF at r.t using quartz cell with a path length of 1 cm.

Complex	λ_{max} /nm (ε /L.mol^{-1}.cm^{-1})
0.5 mM $[Fe(AAN)(H_2O)_2]$ with 1eq $V_2^{2+}.2PF_6^-$	324(2090), 439(200)
reduced 0.5 mM $[Fe(AAN)(H_2O)_2]$ with 1eq $V_2^{2+}.2PF_6^-$	315(4080), 403(1115), 878(1800)
0.5 mM $[Fe(AAN)(H_2O)_2]$ with 2eq $V_2^{2+}.2PF_6^-$	324(3635), 421(555)
reduced 0.5 mM $[Fe(AAN)(H_2O)_2]$ with 2eq $V_2^{2+}.2PF_6^-$	326(4460), 405(1400), 879(1635)
0.5 mM $[Fe(ACl)(H_2O)_2]$ with 1eq $V_2^{2+}.2PF_6^-$	300(340), 353(1380), 390(880)
reduced 0.5 mM $[Fe(ACl)(H_2O)_2]$ with 1eq $V_2^{2+}.2PF_6^-$	301(3925), 429(1290), 885(1575)
0.5 mM $[Fe(ACl)(H_2O)_2]$ with 2eq $V_2^{2+}.2PF_6^-$	300(795), 353(1330), 390(810),
reduced 0.5 mM $[Fe(ACl)(H_2O)_2]$ with 2eq $V_2^{2+}.2PF_6^-$	304(3985), 417(1245), 880(1265)
0.5 mM $[Co(AAN)(H_2O)_2]$ with 1eq $V_2^{2+}.2PF_6^-$	326(2260), 386(780)
reduced 0.5 mM $[Co(AAN)(H_2O)_2]$ with 1eq $V_2^{2+}.2PF_6^-$	316(4785), 403(1185), 882(1270)
0.5 mM $[Co(AAN)(H_2O)_2]$ with 2eq $V_2^{2+}.2PF_6^-$	327(3190), 386(845)
reduced 0.5 mM $[Co(AAN)(H_2O)_2]$ with 2eq $V_2^{2+}.2PF_6^-$	325(4460), 406(1555), 885(1190)
0.5 mM [Ni(AAN)] with 1eq $V_2^{2+}.2PF_6^-$	359(3780), 386(1500), 583(60)
reduced 0.5 mM [Ni(AAN)] with 1eq $V_2^{2+}.2PF_6^-$	532(4810), 830(2640), 747(2290)
0.5 mM [Ni(AAN)] with 2eq $V_2^{2+}.2PF_6^-$	359(2840), 386(1260), 583(55)
reduced 0.5 mM [Ni(AAN)] with 2eq $V_2^{2+}.2PF_6^-$	528(3240), 853(1805), 755(1480)

The non-dimerized viologen radicals absorbed generally at 400 nm (or above) and 600 (or above), while the π-dimerized viologen radicals are characterized by absorptions less than 400 nm, less than 600 nm, and up to 800 nm. The reduced solutions of adducts complexes [Fe(AAN)($V_2^{2+}.2PF_6^-$).Y], [Fe(ACl)($V^+A.PF_6^-$).Y], and [Co(AAN)($V_2^{2+}.2PF_6^-$).Y] showed absorptions at 403 nm and 405 nm; ~400 nm and ~400 nm; 403 nm and 406 mm, respectively. These absorptions are assigned to non-dimerized viologen radicals within adducts complexes, while the absorptions at 878 nm and 879 nm; 885 nm and 880 nm; 882 nm, and 885 nm, respectively, are due to the intra - or intermolecular π-dimerized viologen radicals V_2 within the same adducts complexes (Scheme 7). The reduced mixtures of [Ni(AAN)] with 1 and 2 equivalents of $V_2^{2+}.2PF_6^-$ showed absorptions at 532 nm and 830; 528 nm and 853 nm, respectively. These absorptions correspond to intra- or intermolecular dimrized viologen radicals V_2 within adduct complex [Ni(AAN)($V_2^{2+}.2PF_6^-$).Y], as displayed in Scheme 8 [8,26].

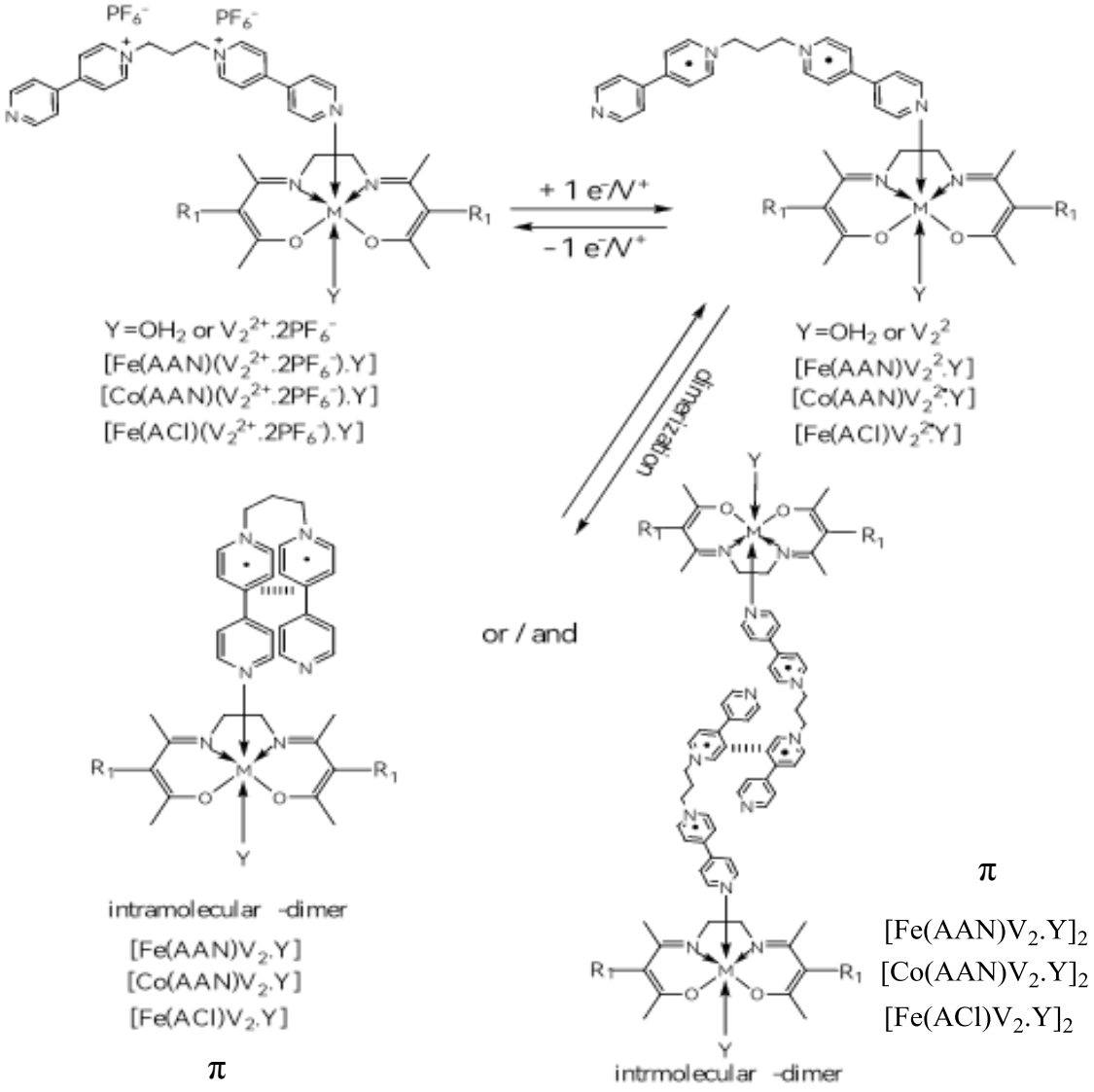

SCHEME 7 Formation of molecular switches from reduction of the adducts complexes [Fe(AAN)($V_2^{2+}.2PF_6^-$).Y], [Fe(ACl)($V_2^{2+}.2PF_6^-$).Y], and [Co(AAN)($V_2^{2+}.2PF_6^-$).Y].

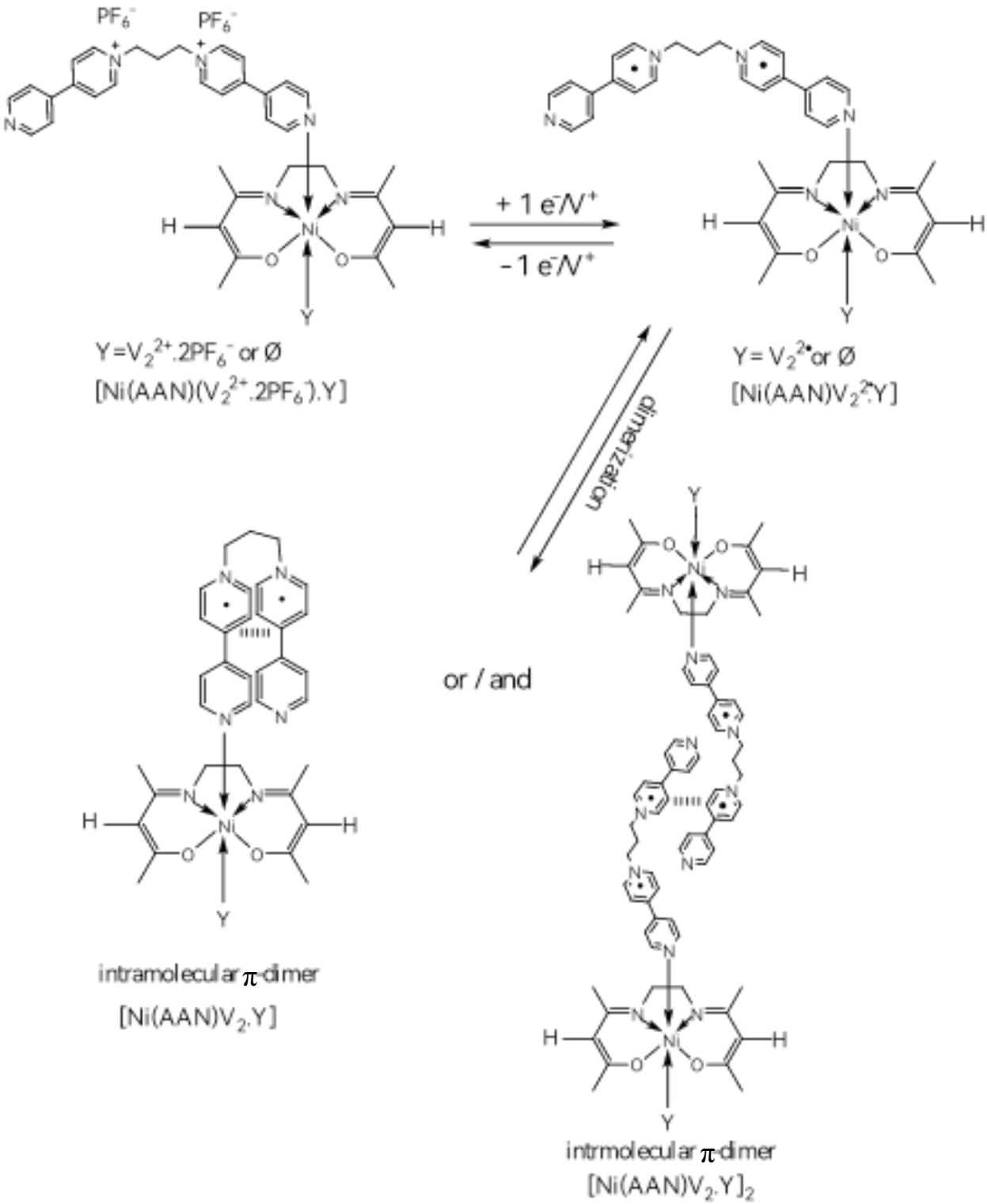

SCHEME 8 Formation of molecular switches from reduction of the adduct complex [Ni(AAN)($V_2^{2+}.2PF_6^-$).Y].

Conclusion

The coordination of H_2O molecules in Fe(AAN), Fe(ACl), and Co(AAN) was confirmed by IR spectroscopy, as was bpy in Fe(AAN)(bpy). IR spectra show the stretching of the M-O group. Thermal analyses showed that the order of thermal stability of complexes decreased in the following sequence:

[Fe(AAN)$(H_2O)_2$] < [Ni(AAN)] < [Fe(ACl)$(H_2O)_2$] < [Co(AAN)$(H_2O)_2$].

All TG phases are first order reactions. During thermal analyses the kinetic and thermodynamic parameters are calculated for each phase. Values obtained for each phase indicate that all phases are non-spontaneous endothermic reactions. Based on XRD data, crystal sizes D are calculated using both the Scherer's and Williamson-Hall methods. Also, the strain values are calculated using the last method. The UV-Visible absorption spectra of complexes in different solvents showed transitions attributed to $\pi - \pi^*$ merged $n - \pi^*$ absorptions. The $d - d$ transitions have been perfectly shown. A comparison of the spectra of the adduct Fe(AAN)(bpy) with those of the precursor Fe(AAN) confirms its formation. UV-visible absorption spectroscopy is used to monitor the formation of adduct complexes from complex interactions with bpy. The adduct complexes $V_2^{2+}.2PF_6^-$ are formed. The $V_2^{2+}.2PF_6^-$ units in these adducts are reduced by two electrons to afford dimerized V_2 within adduct complex structures.

Acknowledgements

Thanks and appreciation to my supervisor, professor, Dr. Wathiq Sattar, who did not spare me his valuable information and support me throughout the research period.

Conflict of Interest

The authors declare no conflict of interest.

Orcid:

Akram Muhamed Musaa:
https://orcid.org/0000-0002-6979-764X
Wathiq Star Abdul-Hassan:
https://orcid.org/0000-0003-1297-3822

References

[1] J. Kumar, A. Rai, V. Raj, A comprehensive review on the pharmacological activity of Schiff base containing derivatives, *Organic & Medicinal Chemistry International Journal*, **2017**, *1*, 88-102. [Crossref], [Google Scholar], [Publisher]

[2] A.H. Gatea, W.S. Abdul-Hassan, S.A. Ali, Z.M. Mahdi, Ligand adducts of bis (acetylacetonato) copper (II), bis (3-chloroacetylacetonato) copper (II) with 4, 4'-bipyridine, and propylene spacered bis-viologen, *J. Med. Chem. Sci.*, **2023**, *6*, 280-303. [Crossref], [Google Scholar], [Publisher]

[3] S. Mehrpour, A. Najafi, A. Ahmadi, T. Zarei, V. Pleqi, K. Basiri, K. KomLakh, H. Abdollahi, K.H. Emami, Relationship of the optic nerve sheath diameter and repeated invasive intracranial pressure measures in traumatic brain injury patients; a diagnostic accuracy study, *Front. emerg. med.*, **2022**, *6*, e6. [Crossref], [Google Scholar], [Publisher]

[4] P.G. Cozzi, Metal–Salen Schiff base complexes in catalysis: practical aspects, *Chem. Soc. Rev.*, **2004**, *33*, 410-421. [Crossref], [Google Scholar], [Publisher]

[5] K. Masaaki, T. Hideki, T. Masanobu, N. Kiyohiko, Tetradentate Schiff base–oxovanadium(IV) complexes: structures and reactivities in the solid state, *Coord. Chem. Rev.*, **2003**, *237*, 183-196. [Crossref], [Google Scholar], [Publisher]

[6] J. Costamagna, J. Vargas, R. Latorre, A. Alvarado, G. Mena, Coordination compounds of copper, nickel and iron with Schiff bases derived from hydroxynaphthaldehydes and salicylaldehydes, *Coord. Chem. Rev.*, **1992**, *119*, 67-88. [Crossref], [Google Scholar], [Publisher]

[7] M. Lersch, M. Tilset, Mechanistic aspects of C– H activation by Pt complexes, *Chem. Rev.*, **2005**, *105*, 2471-526. [Crossref], [Google Scholar], [Publisher]

[8] A.H. Gatea, S.A.A. Alshamkhawy, W.S. Abdul-Hassan, Comparison study of cloud point and solvent extraction of copper by 3-chloro-2,4-pentanedione as complexing agent, *J. Med. Chem. Sci.*, **2022**, *5*, 743-752. [Crossref], [Google Scholar], [Publisher]

[9] C.R. Smith, Activated zinc dust, *Synlett.*, **2009**, *2009*, 1522-1523. [Crossref], [Google Scholar], [Publisher]

[10] L. Eddaif, A. Shaban, J. Telegdi, I. Szendro, A piezogravimetric sensor platform for sensitive detection of lead (ii) ions in water based on calix [4] resorcinarene macrocycles: synthesis, characterization and detection, *Arab. J. Chem.*, **2020**, *13*, 4448-4461. [Crossref], [Google Scholar], [Publisher]

[11] E.R. Agharia, Infrared spectroscopic investigations of effect of strong resonance stabilized intramolecular hydrogen bonding in 1-(1-Hydroxy-2-naphthyl)-3-(phenyl or substituted phenyl-(prop-2-en-1-ones and on their complexation with some transition metals, *Chem. Sci.*, **2015**, *4*, 463-477. [Crossref], [Google Scholar], [Publisher]

[12] M.A. Farrukh, K.M. Butt, K.K. Chong, W.S. Chang, Photoluminescence emission behavior on the reduced band gap of Fe doping in CeO_2-SiO_2 nanocomposite and photophysical properties, *J. Saudi Chem. Soc.*, **2019**, *23*, 561-575. [Crossref], [Google Scholar], [Publisher]

[13] K.Y. Qader, R.A. Ghazi, A.M. Jabbar, K.H. Abass, S.S. Chiad, Reduce of energy gap of Cuo nano structure film by Ag doping, *J. Green Eng.*, **2020**, *10*, 7387-7398. [Google Scholar], [Publisher]

[14] G.M. Poralan, J.E. Gambe, E.M. Alcantara, R.M. Vequizo, X-ray diffraction and infrared spectroscopy analyses on the crystallinity of engineered biological hydroxyapatite for medical application, *IOP. Conf. Ser. Mater. Sci. Eng.*, **2015**, 12028. [Crossref], [Google Scholar], [Publisher]

[15] M. Rabiei, A. Palevicius, A. Monshi, S. Nasiri, A. Vilkauskas, G. Janusas, Comparing methods for calculating nano crystal size of natural hydroxyapatite using X-ray diffraction, *Nanomaterials*, **2020**, *10*, 1-21. [Crossref], [Google Scholar], [Publisher]

[16] N.K. Chaudhary, B. Guragain, S.K. Chaudhary, P. Mishra, Schiff base metal complex as a potential therapeutic drug in medical science: A critical review, *Bibechane.*, **2021**, *18*, 214-230. [Crossref], [Google Scholar], [Publisher]

[17] S.K. Mishra, H. Roy, A.K. Lohar, S.K. Samanta, S. Tiwari, K. Dutta, A comparative assessment of crystallite size and lattice strain in differently cast A356 aluminium alloy, *IOP. Conf. Ser. Mater. Sci. Eng.*, **2015**, 12001. [Crossref], [Google Scholar], [Publisher]

[18] W.S. Abdul-Hassan, D. Roux, C. Bucher, S. Cobo, F. Molton, E. Saint-Aman, G. Royal, Redox-triggered folding of self-assembled coordination polymers incorporating viologen units, *Chem. A Eur. J.*, **2018**, *24*, 12961-12969. [Crossref], [Google Scholar], [Publisher]

[19] M. Ahmadi, S. Seiffert, Coordination Geometry preference regulates the structure and dynamics of metallo-supramolecular polymer networks, *Macromoleculars*, **2021**, *54*, 1388-1400. [Crossref], [Google Scholar], [Publisher]

[20] A.I. Adeogun, N.W. Odozi, N.O. Obiegbedi, O.S. Bello, Solvents effect on nπ* and π* transition of 9-fluorenone, *Afr. J. Biotechnol.*, **2005**, *4*, 2736-2738. [Pdf], [Google Scholar], [Publisher]

[21] X. Liu, K. Neoh, L. Zhao, E. Kang, Surface functionalization of glass and polymeric substrates via graft copolymerization of viologen in an aqueous medium, *Langmuir*, **2002**, *18*, 2914-2921. [Crossref], [Google Scholar], [Publisher]

[22] W.S. Abdul-Hassan, E. Saint-Aman, G. Royal, C. Kahlfuss, C. Bucher, Molécules et matériaux moléculaires redox- et photo-stimulables, *L'Actualité Chimique*, **2018**, *430*, 79-84. [Google Scholar], [Publisher]

[23] J. Courtois, B. Wang, W.S. Abdul-Hassan, L. Almasy, M. Yan, G. Royal, Redox-responsive colloidal particles based on coordination polymers incorporating viologen units, *Inorg. Chem.*, **2020**, *59*, 6100-6109. [Crossref], [Google Scholar], [Publisher]

[24] R. Soury, M. Jabli, T.A. Saleh, W.S. Abdul-Hassan, E. Saint-Aman, F. Loiseau, C.

Philouze, H. Nasri, Tetrakis (ethyl-4 (4-butyryl) oxyphenyl) porphyrinato zinc complexes with 4, 4′-bpyridin: synthesis, characterization, and its catalytic degradation of Calmagite, *RSC Adv*., **2018**, *8*, 20143-20143-20156. [Crossref], [Google Scholar], [Publisher]

[25] T. Sakano, F. Ito, T. Ono, O. Hirata, M. Ozawa, T. Nagamura, Synthesis and electrochromic properties of a highly water-soluble hyperbranched polymer viologen, *Thin Solid Films*, **2010**, *519*, 1458-1463. [Crossref], [Google Scholar], [Publisher]

[26] S. Chowdhury, C. Kahlfuss, D. Frath, F. Chevallier, E. Dumont, G. Royal, E. Saint-Aman, C. Bucher, Dynamic molecular metamorphism involving palladium-assisted dimerization of π-cation radicals, InGECOM CONCOORD 2019 May 19. [Crossref], [Google Scholar], [Publisher]

How to cite this article: Akram Muhamed Musaa*, Wathiq Star Abdul-Hassan. Iron (II), Cobalt (II), and Nickel (II) complexes of bis- (3-chloroacetylacetonate) ethylenediimine and bis-(acetylacetonate) Ethylenediimine and their viologen molecular switches. *Journal of Medicinal and Pharmaceutical Chemistry Research*, 2023, 5(6), 492-521.